

# Interpreting the Morphology of Diffuse Light Around Satellite Galaxies

Kathryn V. Johnston

Van Vleck Observatory, Wesleyan University, Middletown, CT 06459

E-mail: kvj@astro.wesleyan.edu

Philip I. Choi, Puragra Guhathakurta

UCO/Lick Observatory, University of California, Santa Cruz, CA 95064

E-mail: pchoi@ucolick.org, raja@ucolick.org

## ABSTRACT

Recent observations of surface brightness distributions of both Milky Way and M31 satellite galaxies have revealed many instances of sudden changes or breaks in the slope of the surface brightness profiles (at some break radius,  $r_{\text{break}}$ ). These breaks are often accompanied by increasingly elliptical isophotes and sometimes by isophote twisting. We investigate the hypothesis of a tidal origin for these features by applying the same ellipse fitting techniques that are used on observed galaxies to numerical simulations of the destruction of satellites, represented by spherical, single-component systems. We examine how observed quantities such as  $r_{\text{break}}$ , ellipticity  $e$  and position angle  $\phi$  of the fitted ellipses and amplitude of extra-break population vary with the satellite's orbital eccentricity and phase, and our viewpoint relative to the orbit. We also look at orbit and viewpoint dependence of the rate of change of the latter three quantities with radius.

We find that there are trends with orbital phase and eccentricity in all observed quantities, many of which are preserved through a wide variety of viewing angles. In particular, a generic feature of all simulations is a depletion zone just interior to an excess zone, regions in which the surface brightness is lower and higher, respectively, than the initial profile. A clear interpretation of any individual image, however, is likely to be hampered by the dependence of the observable features on these multiple parameters. For example, breaks can be excited by several physical processes and can occur well within the bound satellite population. Nevertheless, we do find we can place loose constraints on the tidal radius, mass loss rate, orbital type and phase of the satellite, and nature of breaks using photometric data alone.

*Subject headings:* methods: n-body simulations — galaxies: dwarf — galaxies: interactions — galaxies : evolution

## 1. Introduction

The surface brightness distributions of Galactic globular clusters and dwarf spheroidal satellites have traditionally been studied using star count data. In the last few years, very low surface brightness levels have been reached by removing contaminants either by making use of a survey that covers a significant area around the satellite so the background counts can be assessed (Irwin & Hatzidimitriou 1995), making some color cuts (Gould et al. 1992; Grillmair et al. 1995; Leon, Meylan & Combes 2000) or concentrating on specific classes of associated stars such as RR Lyrae (Kuhn, Smith & Hawley 1996) or metal-poor giants (Majewski et al. 2000). These approaches have revealed many instances of the slope of a satellite’s surface brightness profile abruptly changing at some radius  $r_{\text{break}}$ , so that the satellite is apparently surrounded by a diffuse envelope of stars (see Grillmair, 1998, for a more complete listing). In some instances, this break is accompanied by distortions and twisting of the star count isopleths, and even hints of a stream of debris extending along a particular axis (Leon, Meylan & Combes 2000; Odenkirchen et al. 2000).

Grillmair et al. (1996) report indications of tidal debris around some of M31’s globular clusters using HST to perform a similar star count analysis. However, to reach such low surface brightness levels around satellites of external galaxies in general will mean working in integrated light rather than individual star counts. We can get a sense for the sensitivity required by noting that debris found using star counts separated from Sagittarius by 10–40 degrees has been estimated to correspond to steadily decreasing surface brightnesses in the range  $\mu_V \sim 27\text{--}30\text{ mag arcsec}^{-2}$  (Mateo, Olszewski & Morrison 1998). Clearly, the surface brightness of debris will depend on the mass loss rate and orbit of the satellite — for example, the giant star count densities reported recently in Majewski et al. (2000) around Carina correspond to a drop of roughly a factor of 100 from their central value, or  $\mu_V \sim 30\text{ mag arcsec}^{-2}$ . In Choi, Guhathakurta & Johnston (2002) we present the results of work where we find low surface brightness features similar to the extra-break populations of the Milky Way’s satellites around satellites of M31: NGC 205 and M32. This was made possible by a wide-field CCD image of M31, a mosaic of 60 precisely flat-fielded and sky-subtracted frames (Guhathakurta, Choi & Raychaudhury 2002), which allowed the careful subtraction of M31’s light from the fields around NGC 205 and M32. This approach allowed for the extension of work by Hodge (1973) and Kent (1987) to surface brightness limits of  $\mu_B \sim 27\text{ mag arcsec}^{-2}$ .

These “extra-break” features are reminiscent of particle distributions seen in simulations of the destruction of a satellite in a tidal field (Grillmair et al. 1995; Johnston, Sigurdsson & Hernquist 1999; Combes, Leon & Meylan 1999). Clearly this work is closely related to the vast literature on signatures of mergers of galaxies such as tidal tails (Toomre &

Toomre 1972) and shells (Quinn 1984). The advantage of looking at satellite galaxies is that their influence on their parent is negligible and this simplifies the dynamics of the debris considerably. Once lost from the satellite, debris in these simulations is seen to spread along the orbit of the satellite in thin streams at a predictable rate (Tremaine 1993; Johnston 1998; Helmi & White 1999). This has led to the suggestion that the morphology of extra-break populations can be used to constrain the direction in which the satellite is moving (Grillmair et al. 1995; Combes, Leon & Meylan 1999), which in turn could tell us something about the satellite’s orbit — information that is useful for both understanding the satellite’s history and for comparing orbital distributions of a galaxy’s satellite system with cosmological models (Tormen, Bouchet, & White 1997; Ghigna et al 1998). Other work has shown that the surface density of the debris can be used to estimate the mass-loss rate from the satellite (Johnston, Sigurdsson & Hernquist 1999), and that the limitation of the satellite or extent of debris gives some indication of the satellite’s mass and hence dark matter content (Faber & Lin 1983; Kuhn & Miller 1989; Kuhn 1993; Moore 1996; Burkert 1997; Klessen & Kroupa 1998).

In light of this steady stream of results on extra-break populations from within and beyond the Milky Way, the aim of this paper is to confirm and generalize some of the theoretical ideas of earlier studies. In particular, we are interested not in how or why a satellite is disrupting, but rather in what general statements we can make about its state and past evolution by observing its debris. Our current intuition is that: (i) the physical scale (corresponding to  $r_{\text{break}}$ ) over which debris is distributed is proportional to the ratio  $(m_{\text{sat}}/M_{\text{gal}})^{1/3}$ , where  $m_{\text{sat}}$  is the satellite’s mass and  $M_{\text{gal}}$  is the parent galaxy mass enclosed within the pericenter of the satellite’s orbit (Johnston 1998); (ii) as long as we scale the size of any box we are considering around the satellite by this ratio, the morphology (i.e. two-dimensional shape and one-dimensional profile) of the extra-break population will depend only on orbital eccentricity, orbital phase and viewpoint; and (iii) the amplitude of the surface-density of the extra-break population is proportional to the mass-loss rate from the satellite (Johnston, Sigurdsson & Hernquist 1999). The mass loss rate itself will vary with the orbit and density structure of the satellite (Weinberg 1994a,b,c; Johnston, Hernquist & Bolte 1996), but we do not study these dependencies directly since they will only affect the amplitude and not the overall morphology of the extra-break population. We instead focus on hypotheses (ii) — the dependencies that have been explored the least — by looking at simulations of satellites being destroyed along orbits with a variety of eccentricities and viewed at all orbital phases along many directions.

We have a particular interest in the appearance of companions to external galaxies, at sufficiently large distance from their parents that their surroundings can be studied (Choi, Guhathakurta & Johnston 2002). Hence we closely mimic observational work by projecting

particle positions onto a grid and then analyzing this “CCD” image with standard IRAF routines. Finally, we compare the appearance of our fitted ellipses to the known conditions in our simulated satellite, with the intention of relating observables to the satellite’s physical state.

We present our numerical and analysis methods in §2, examine the relationship between observable features in the surface brightness distribution and the physical state of the satellite in §3 and discuss how to interpret extra-break populations in §4. We summarize our results in §5.

## 2. Methods

### 2.1. The Simulations

#### 2.1.1. Technique

This paper is based on an analysis of five simulations of tidal disruption (hereafter Models 1–5) run using the technique described in Johnston, Hernquist & Bolte (1996). The parent galaxy is taken to be smooth, static and axisymmetric, and is represented by a three-component model, in which the disk is described by the Miyamoto-Nagai (1975) potential, the spheroid by a Hernquist (1990) model, and the halo by a logarithmic potential:

$$\Phi_{disk} = -\frac{GM_{disk}}{\sqrt{R^2 + (a + \sqrt{z^2 + b^2})^2}}, \quad (1)$$

$$\Phi_{spher} = -\frac{GM_{spher}}{r + c}, \quad (2)$$

$$\Phi_{halo} = v_{halo}^2 \ln(r^2 + d^2). \quad (3)$$

We take  $M_{disk} = 1.0 \times 10^{11}$ ,  $M_{spher} = 3.4 \times 10^{10}$ ,  $v_{halo} = 128$ ,  $a = 6.5$ ,  $b = 0.26$ ,  $c = 0.7$ , and  $d = 12.0$ , where masses are in  $M_{\odot}$ , velocities are in km/s and lengths are in kpc. This choice of parameters yields a nearly flat rotation curve at  $\sim 200$ km/s between 1 and 30 kpc and a disk scale height of 0.2 kpc. The radial dependence of the vertical epicyclic frequency of the disk ( $\kappa_z$ ) between 3 and 20 kpc is similar to that of an exponential disk with a 4 kpc scale length. Although this model was constructed to represent the Milky Way specifically, we anticipate our general results will be applicable to any satellite/parent galaxy pair by using the scaling factor  $(m_{sat}/M_{Gal})^{1/3}$  described in §1.

The satellite is represented by 64,000 particles whose mutual interactions are calculated using a code developed by Hernquist & Ostriker (1992) and based on the basis-function-

expansion technique. In Models 1–4 the satellite particles are initially distributed as a Plummer model (Binney & Tremaine 1987), and in Model 5 as a Hernquist (1990) model (as illustrated in 1). The total mass of the satellite in each case is  $10^8 M_\odot$ , the scale length is 0.5 kpc, and all are on orbits with pericenters at 30 kpc. In Model 1/2/3/4/5 the satellite’s orbit has an apocenter of 37/55/150/450/450 kpc corresponding to a radial orbital time period (i.e. time between successive pericenters) of 0.76/0.96/2.2/6.0/6.0 Gyr. In each case, the satellite is followed for a total of 5 radial orbits, with 50 snapshots saved on each orbit to allow the morphology to be analyzed as a function of orbital phase. Note that each satellite maintained a core of bound particles throughout the simulations (no satellite lost more than 60% of its mass during the 5 orbits).

### 2.1.2. Limitations of Model and Parameter Choices

This study is concerned with the appearance of slowly disrupting, low mass satellites on orbits that do not interact significantly with any disk components of the parent galaxy. We expect similar features (though a different dependence on orbital phase) around satellites which have lost mass through disk shocking (see Combes, Leon & Meylan, 1999, for a detailed discussion).

Our parent galaxy was represented by a static potential. We do not follow its response to the satellite and hence cannot assess the dynamical influence of that response on the satellite and associated debris. We are instead interested in features in the vicinity of the satellite, where debris, once unbound, disperses within an orbital time. As long as the satellite is not massive enough for its orbit to decay significantly within this timescale we expect our static potential approximation will not affect the morphology and interpretation of such local debris. The requirement of the orbital timescale being less than the dynamical friction timescale corresponds to an upper limit on the mass of the satellite (estimating  $T_{\text{orb}} = 2\pi R/v_{\text{circ}}$  and re-arranging equation [7-27] from Binney & Tremaine, 1987):

$$m_{\text{sat}} < \left( \frac{v_{\text{circ}}}{220 \text{ km s}^{-1}} \right)^2 \left( \frac{R}{60 \text{ kpc}} \right) \frac{1}{\ln \Lambda} 10^{11} M_\odot, \quad (4)$$

where  $v_{\text{circ}}$  is the parent galaxy’s circular velocity,  $R$  is the distance between parent and satellite galaxies and  $\ln \Lambda$  is the Coulomb logarithm (which has typical values of  $\ln \Lambda \sim 3 - 10$  — see Binney & Tremaine, 1987).

We do not consider non-spherical satellites since the force-field a star experiences in the extra-break region is dominated by the monopole moment of the satellite combined with the tidal field of the parent galaxy and is largely independent of the satellite’s internal structure.

This argument will break down if the satellite is far from spherical and our results should not be applied to disk systems.

We only consider non-rotating satellites. The population of debris orbits will depend on the population of orbits within the satellite and this will influence the morphology in the extra-break region, so our results will not be directly applicable to systems with significant rotation.

Finally, we use single component models, which corresponds to assuming a constant mass-to-light ratio throughout the system. We expect that a mass-to-light ratio that decreases with distance from the center of the satellite would change the surface brightness profile, but not the ellipticity or orientation of the fitted ellipses. This intuition will be tested in future work.

## 2.2. Analysis

This paper is written as a companion to the observational work described in Choi, Guhathakurta & Johnston (2002) and the analysis performed is designed to mimic that study as closely as possible. In this section we describe the analysis performed on each snapshot, and illustrate the the results with snapshot 121 of Model 1, viewed at 90 degrees to the orbital plane of the satellite.

### 2.2.1. *Fitting isophotes*

To get ‘surface brightness’ distributions for each snapshot the particle positions are first projected onto the parent galaxy’s rest frame in a coordinate system centered on the satellite. Projections with viewing angles of 0, 30, 60 and 90 degrees to the orbital plane are used. For a given viewing angle, projected particle positions are binned into a two-dimensional grid of 20 pc×20 pc bins. Note that although the resulting frames contain no conventional observational noise, they are limited by discreteness effects due to the finite number of particles. To overcome this, the grids are smoothed using a 200 pc sigma gaussian kernel. Ellipses are then fit to the ‘isophotes’ (isopleths) of the smoothed snapshots using the IRAF/STSDAS task ELLIPSE.

Figure 2 is a grayscale image of a smoothed snapshot (frame 121) from Model 1 that has been overlaid with ellipse fits in red.

### 2.2.2. Characterizing Each Snapshot

Given our sample of 250 snapshots from each model it is impossible to consider each one separately. Instead we define a number of quantities to summarize the general characteristics of each snapshot. As an example, Figure 3 shows the results of the isophotal analysis applied to Snapshot 121 of Model 1.

The top panel of Figure 3 plots the surface density  $\Sigma$  as a function of ellipse semi-major axis  $a$ . We fit lines to the seven points (spanning nearly a factor of two in radius) defining the profile both interior and exterior to each fitted ellipse and find the difference in the slopes of the lines  $\Delta\gamma(a) = \gamma_{\text{xt}} - \gamma_{\text{in}}$ . Local maxima and minima of  $\Delta\gamma$  are identified and  $r_{\text{break}}$  is taken to be the innermost turning point with  $|\Delta\gamma| > \Delta\gamma_{\text{lim}}$ . We adopt a standard value of  $\Delta\gamma_{\text{lim}} = 0.2$  — the dependence of results of this analysis on the limit used will be discussed in §3.2. Note that this approach means that no breaks can be found beyond  $a \sim 5$  kpc in our  $20 \text{ kpc} \times 20 \text{ kpc}$  analysis box — we repeat the analysis on a larger box in cases where no break is found within 5 kpc. The second panel emphasizes the breaks by plotting the difference between the current and the initial brightness profiles.

The lower panels of Figure 3 show the run of ellipticity  $e$  and position angle  $\phi$  with semi-major axis of the fitted ellipses. The position angle is measured relative to the line joining the satellite and the parent galaxy center, defined to be positive towards the satellite’s projected direction of motion. [This sign convention breaks down when the viewpoint is along the plane of the satellite’s orbit, but that is unimportant since there is no isophote twisting in this case (see §3.5).] Once  $r_{\text{break}}$  is defined (as described in the previous paragraph) the rate of change of each of these quantities ( $\gamma_e$  and  $\gamma_\phi$ , indicated by the solid lines in the figure) with  $a$  is characterized by fitting straight lines to the points in the region  $r_{\text{break}} < a < 2r_{\text{break}}$ .

Although the break in the surface density is the most striking feature in the upper panel it is noticeable that the satellite loses its intrinsically spherical shape well within this point. To indicate the innermost point where the morphology might be affected by tidal forces we also record the innermost semi-major axis at which  $e > 0.02$ , hereafter referred to as  $r_{\text{distort}}$ . For intrinsically elliptical satellites  $r_{\text{distort}}$  can instead be identified as the point where the ellipticity and alignment of isophotes start changing significantly.

## 2.3. Relationship between Observables in Simulations Versus Real Galaxies

By analogy with real galaxies, we are restricted to looking for profile breaks — it would be unrealistic, for example, to study departures from the intrinsic/initial profile. Real galaxies have complicated profiles so it is easier in general to look for extreme breaks (say with

$\Delta\gamma_{\text{lim}} = 1.0$ ) than subtle ones ( $\Delta\gamma_{\text{lim}} = 0.2$ ). While we explore the use of different  $\Delta\gamma_{\text{lim}}$  in §3.2 and in Figures 8 and 15–17, most of the analysis in the paper is based on  $\Delta\gamma_{\text{lim}} \sim 0.2$ , since the resulting observables in the simulations display cleaner trends as a function of orbital eccentricity, orbital phase, and intrinsic profile shape.

In considering the ellipticity and position angles of the model galaxy isophotes, it is important to note that real galaxies typically have intrinsically non-circular isophote shapes. This makes it more difficult to measure ellipticity changes and isophote twists for real galaxies than for simulated ones — while the ellipticity is a monotonically increasing function of radius for simulated galaxies, one should not expect the same trend in real galaxies.

### 3. Results

A tidal field imposed on a satellite can: (i) heat stars within the satellite; (ii) strip stars from the satellite once they have been sufficiently heated; and (iii) cause stripped stars to disperse away from the satellite along its orbit. The satellite will respond to these adjustments in its internal phase-space distribution by attempting to relax to a new equilibrium. All of these effects can alter the surface brightness profile and shape of the satellite, but we expect the nature of this evolution to depend both on the orbit and the orbital phase at which it is observed. Along circular orbits tidal heating, stripping and debris dispersal are steady processes. For orbits that are progressively more eccentric, a larger fraction of heating and mass loss occurs during a smaller fraction of the orbit around pericenter. The rate of debris dispersal is also largest around pericenter. The density of debris at any time around the satellite is influenced in opposite senses by all these effects and hence is hard to predict analytically. For example, on highly eccentric orbits debris rapidly disperses away from pericenter and congregates near apocenter, where the orbital speed is lowest, so that the debris density is highest near apocenter despite the predominance of mass loss around pericenter. In contrast, the relaxation of the satellite depends only on its internal structure and is independent of its orbit.

In the following subsections we examine how observations can be interpreted in terms of this physical picture of heating, stripping, debris dispersal and relaxation.

#### 3.1. Break Radii

In this section we investigate how we can relate the appearance of breaks in the surface density profile to the physical picture outlined above in order to develop some intuition for



the cause of the phase and orbit dependence of observed distortions.

### 3.1.1. Morphology of Debris Around a Satellite

We begin by contrasting the morphology of particles that are still bound, those that are in the process of being stripped from the satellite and those that have been lost from the satellite for more than one orbit. We label the particles with the number of the orbit (defined apocenter to apocenter) during which they became unbound from the satellite. [At each time step in the simulation, we define a particle’s binding energy relative to the satellite using the technique outlined in Johnston, Sigurdsson & Hernquist (1999): the parent galaxy potential is ignored and the binding energy is calculated from the potential energy of the satellite and kinetic energy of motion relative to the satellite.] Figure 4 illustrates the results of this division of the particles into separate “debris populations” with a set of projections of particle positions onto the orbital plane for a series of snapshots taken from the third radial orbit of each model (equally spaced between the third and fourth apocenters) The particles are coded green/cyan/blue/red/yellow if they were (are being/will be) lost during orbits 1/2/3/4/5 (those not lost during these orbits are not shown). In each panel, the negative  $Y$  axis points in the direction of the parent galaxy and the dotted box indicates the region over which the analysis was performed. Each panel is  $80 \text{ kpc} \times 80 \text{ kpc}$ . Figure 5 zooms in on the  $20 \text{ kpc} \times 20 \text{ kpc}$  analysis boxes indicated by the dotted lines in Figure 4. In these panels the ellipse indicates the isophote corresponding to the innermost break radius identified with  $\Delta\gamma_{\text{lim}} \sim 0.2$  (hereafter simply referred to as  $r_{\text{break}}$ ) and the line shows the direction of motion of the satellite. No ellipse is drawn in the second panel of Model 5 since no break with  $\Delta\gamma > 0.2$  was found within the analysis box for this snapshot.

Three trends in the morphology of debris populations are worth noting in Figures 4 and 5. First, it is clear that the extent of the particle distributions are similar near pericenter (middle row of panels) as all models are experiencing the same potential field at this orbital phase. As the distance from the center of the galaxy increases, the potential field becomes weaker and hence the particles are most widely distributed at the apocenters of the most eccentric orbits. Second, although the density of unbound (green and cyan) particles around Model 4 is always lower than Model 5, the panels appear otherwise morphologically similar. Recall that these models both follow the same orbit and differ only in their initial satellite profiles. The difference in density reflects the lower mass loss rate from Model 4, while the similarity in morphology is a consequence of the fact that debris dynamics depends primarily on the satellite mass and orbit and parent galaxy potential and is largely unaffected by the internal structure of a satellite (see §2.1.2). The internal structure *does* affect the

identification of break radii and hence the interpretation of extra-break populations — this will be discussed further in §3.3. Third, in Figure 4 the spatial extent of each population increases steadily for Models 1 and 2 as debris disperses along the orbit. In contrast, although there is an increase in the extent of (for example) the blue population from apocenter to apocenter in Models 3-5, the particles actually spread further along the orbit at pericenter than they do in the final apocenter panels. This difference is a direct consequence of the variable rate of debris dispersal with orbital phase along the more eccentric orbits. Similarly, Helmi & White (1999) found peaks in the density at the center of the remnant of a destroyed satellite at both pericenter and apocenter as well as a general trend for the density to decrease with time. These peaks in density are not so obvious in our plots because of the scale: within each panel we are looking at debris spread around a bound satellite along a range of orbital phases.

### 3.1.2. Appearance and Physical Interpretation of Break Radii

Figure 6 shows the surface density profiles corresponding to each of the panels in Figure 4, with the solid lines indicating  $r_{\text{break}}$ . The stars in the panels for Models 3–5 plot the results of the same analysis run on a  $40 \text{ kpc} \times 40 \text{ kpc}$  box. Figure 7 plots the difference between the current profile and the initial profile at the start of the simulation in order to emphasize the validity of the identification of the shallowest breaks that are not apparent to the eye in Figure 6. It also demonstrates that the profile has evolved significantly away from the initial profile even at radii well within the innermost identified break radius. In particular note that the central surface density decreases ever so slightly but steadily throughout each simulation — a signature of the expansion of the satellite as it relaxes in response to the heating and stripping of its outer regions.

Note also that there are several cases of multiple breaks appearing in a panel. Such features have also been found in simulations of disk shocking of globular clusters (Leon, Meylan & Combes 2000).

Figures 4 and 5 both indicate that although the different debris populations overlap, there are clear boundaries between regions dominated by each set, and these provide a useful backdrop against which to compare  $r_{\text{break}}$ . [This clear separation between particles lost on each pericentric passage is analogous to Combes, Leon & Meylan (1999) finding that each disk passage in their simulations of globular cluster disruption produced distinct overdense “lumps” in their tidal tails.] The left hand panels of Figure 8 assesses which population dominates the surface brightness profile around  $r_{\text{break}}$  by plotting the number of particles in each debris population (color coded in the same way as Figure 4) in the

region where the fitted ellipses have semi-major axes  $0.9r_{\text{break}} < a < 1.1r_{\text{break}}$ . The aim of this figure is to understand whether breaks can be attributed to: *heating* within the still-bound population; the *stripping* of particles from the satellite; or the *transition* between two unbound populations lost on different (consecutive) orbits. Each row of the figure shows the same sequence of colors dominating the particle numbers as each population is heated and stripped in order. However, both the phase at which the different colors become dominant and the ratio of the number of particles in other populations to the dominant one at any given phase are orbit dependent. This variance suggests that there is no unique physical interpretation of breaks in a surface density profile. In the next section, we go on to examine the orbit and phase dependence of break interpretation in more detail.

### 3.2. Dependence on Orbital Eccentricity and Phase

In this section we first examine how the nature of the break in the surface brightness profile at  $r_{\text{break}}$  depends on the orbit of the satellite. We then investigate whether the ellipticity and position angles of the isophotes might allow us to distinguish between breaks caused by different processes. Finally, we look at how general our results are by summarizing the observables as a function of orbital phase for all snapshots from each model. We concentrate exclusively on Models 1–4, which all had the same initial satellite profile. In §3.3 we will go on to examine the dependence on satellite profile by comparing Models 4 and 5.

#### 3.2.1. Orbital Eccentricity

Along near-circular orbits (e.g. Model 1) all panels of Figure 6 show clear breaks above the inner profile, with the extra-break population having similar amplitude and a shallow slope at all phases. Figure 8 shows that our analysis of the extra-break population is dominated by debris lost on the current orbit (blue in Figures 4 and 5) throughout each orbit, with negligible contribution from other populations and sharp transitions between the dominant population just before the apocenter of each orbit. These characteristics indicate that the breaks we have identified generally occur where stripping is actively taking place along circular orbits — heating within the bound population is steady and hence does not cause an identifiable signature in the profile, and the sudden change between bound and dispersing populations causes an abrupt break above the inner profile.

As the orbit becomes more eccentric the extra-break population has varying amplitude and slope, but in general a higher amplitude and steeper slope than the circular case. Figure 8

shows that the transition between the different dominant populations identified around  $r_{\text{break}}$  moves to *earlier* orbital phases for more eccentric orbits. Moreover, the *other* (i.e. non-dominant) populations make an increasing fractional contribution throughout every orbit for increasing orbital eccentricity. In the most extreme cases (e.g. Model 4) the contribution of particles to be lost on the next orbit is of the same order as that of particles currently being stripped. Finally, since most mass loss occurs at pericenter along these eccentric orbits the vast majority of particles labeled as being lost on the current orbit (e.g. the blue particles which dominate for  $2 < t/t_R < 2.5$ ) will still be bound during the first half of the orbit; in the second half of each orbit the dominant population consists of particles to be lost during the next orbit (e.g. the red particles for  $2.5 < t/t_R < 3$ ). These characteristics suggest that the  $r_{\text{break}}$  identified lies well within the still-bound population as a result of shock-heating during the pericentric passages.

Note that additional breaks in the profile beyond  $r_{\text{break}}$  occur in Model 4, at larger radii and with larger  $|\Delta\gamma|$  than those at  $r_{\text{break}}$  (see Figures 6 and 7). Indeed, if we make our condition for break identification more restrictive ( $\Delta\gamma_{\text{lim}} = 1.0$ ), the break identified is often this outer, more-apparent break. The relative dominance of a single (unbound) debris population, rather than a mixture of bound populations, at most orbital phases in the right hand panels of Figure 8 indicate that this outer, more extreme break is more analogous to the breaks caused by stripping as seen in near-circular orbits.

A further example of multiple breaks within a single profile having different interpretation is the fourth panel of Model 3 in Figure 6. Here,  $r_{\text{break}}$  appears to correspond to a point within the satellite that has just been shocked by the pericentric passage. The clear break below the continuation of the surface density at about  $a = 10$  kpc, on the other hand, can be attributed to the morphological differences between the blue and cyan particles (apparent in Figures 4 and 5), or the transition between two unbound populations.

We conclude that breaks in the profiles of objects disrupted along near-circular orbits will usually be due to stripping. Objects on more eccentric orbits are more severely shocked at pericentric passages and can exhibit breaks within their still-bound populations as well as breaks analogous to those seen along near-circular orbits. Unfortunately, the orbit of a satellite is not an observable quantity so the exact interpretation of a break in a profile is ambiguous without some other clues.

### 3.2.2. Relating the Nature of $r_{\text{break}}$ to Other Properties

Additional information can be gleaned from the shape and orientation of the isophotes. Figures 9 and 10 show the run of ellipticity  $e$  and position angle  $\phi$  (with half-sized points showing isophotes with  $e < 0.02$  — i.e.  $r < r_{\text{distort}}$ ) corresponding to each of the panels in Figures 4–7. The solid lines indicate  $r_{\text{break}}$ , which often (although not always) coincides with features in these plots. In general,  $e$  monotonically increases with  $a$  but  $\phi$  does not, suggesting that reversals in the sense of twists in tidal features may be common. Comparing these figures with our earlier interpretation, we find that if  $r_{\text{break}}$  is caused by stripping, then significant ellipticity and twisting of isophotes can occur well within this point (or, equivalently  $r_{\text{break}}/r_{\text{distort}} > 1$  and the full-sized points begin well within the break radius in Figures 9 and 10). If  $r_{\text{break}}$  is caused by heating it more closely corresponds to  $r_{\text{distort}}$ . In the latter case we can also conclude that the satellite is likely to be on an eccentric orbit.

### 3.2.3. Trends in Observables with Orbital Phase

We examine how general the conclusions in the previous sections are by summarizing the “observations” (using quantities defined in §2.2.2) of all the snapshots in the simulations. These are presented in Figures 11 and 12, again viewed along a line of sight perpendicular to the orbital plane. There are clear trends in all quantities with orbital phase, and a large scatter about these trends. The nature of the trends is orbit dependent, with small-amplitude, continuous changes in the case of steady tidal stripping along the near-circular orbit (Model 1) and sudden swings over a progressively smaller fraction of the orbit as the orbital eccentricity increases.

One striking feature in Figure 11 is the increase in  $\gamma_{\text{xt}}$  along the most eccentric orbit (Models 4 and 5) after the pericenter shock followed by the sudden dive to a new  $\gamma_{\text{xt}}$  which remains steady throughout the rest of the orbit — this occurs at the orbital phase clearly corresponding to the transition between dominance by different populations, shown in Figure 8. One interpretation is that the increase is caused by  $r_{\text{break}}$  first tracking the population that has just been unbound at pericenter (so the break at this orbital phase is analogous to the breaks caused by particles being stripped in Models 1 and 2) and then readjusting as the disturbance in the inner profile caused by heating within the bound satellite becomes apparent.

This idea is supported by the general  $e$  and  $\phi$  characteristics seen in Figure 12. Comparing across the orbit types, we find  $e$ ,  $\gamma_e$ ,  $\phi$  and  $\gamma_\phi$  are systematically lower at most phases along the more eccentric orbits since  $r_{\text{break}}$  was identified well within the bound population

of the satellite. The only phase where this is not true corresponds to where we expect stripping to be occurring around  $r_{\text{break}}$ . These characteristics are consistent with our findings in the previous section that breaks in the brightness profile caused by heating tend to occur close to the point where the satellite first becomes deformed by the tidal field (i.e. where  $r_{\text{break}}/r_{\text{distort}} \sim 1$  — see second row of panels in Figure 11), while those caused by stripping can be well outside this region. Thus, our use of spherical satellite models would allow us to attribute the breaks to heating or stripping "observationally" using  $r_{\text{break}}/r_{\text{distort}}$ , since  $r_{\text{distort}}$  always occurs within populations still bound to the satellite. Unfortunately,  $r_{\text{distort}}$  may not be so unambiguously defined in intrinsically elliptical systems, although a similar aim might be fulfilled by looking at the onset of isophote twists (as discussed in §2.2.2).

These plots confirm that though the appearance of breaks is both orbit and orbital phase-dependent, the ellipticity and twisting of isophotes can offer further clues to a physical interpretation.

### 3.3. Dependence on Intrinsic Profile Shape

In Model 5 we repeated a simulation with the same orbit as Model 4 but with a Hernquist rather than a Plummer model satellite. Comparing the relevant panels in Figures 4–12 we find that the characteristics of the debris in both populations are very similar — a reflection of the very similar dynamical influences that particles in both models experience once they are unbound from the satellite. Key differences are that the surface density of the extra-break population is greater and  $\Delta\gamma$  is systematically lower throughout much of Model 5. The former is because the mass loss rate is higher from the satellite in Model 5 — disruption is a density criterion so altering the mass distribution does in general alter the mass loss rate. The latter is because the surface brightness profile of the Hernquist model is shallower than that of the Plummer model, so that breaks are less pronounced. As a consequence, along Model 5 there are instances where no  $r_{\text{break}}$  is identified within the 20 kpc  $\times$  20 kpc grid on which the analysis is performed, even though we expect the debris in this model to behave similarly to that in Model 4. There are also more cases where the break is *below* rather than above the continuation of the inner surface density — these are highlighted with solid boxes in all panels of Figures 11 and 12. These breaks tend to occur well inside the bound satellite population in regions where the satellite is less distorted by the tidal field (i.e. low  $e$  and twists).

The comparison of the two models emphasizes that  $\Delta\gamma$  is a reflection of the initial satellite profile as much as the orbit which the satellite is on. A more reliable indicator of orbital eccentricity is  $\gamma_{\text{xt}}$  which is systematically lower along the more eccentric orbits,

independent of satellite model (Figure 11).

### 3.4. Dependence on Resolution

Near apocenter, Models 3–5 covered significantly larger spatial scales than Models 1–2. In order to examine the outskirts of these models we repeated our analyses within a  $40\text{ kpc} \times 40\text{ kpc}$  box, effectively degrading our pixel scale by a factor of two (results shown as stars in Figure 6). We found that the “observables” on this larger grid were similar to their counterparts on the nominal grid (latter shown in Figures 11 and 12). However, the larger grid scale did smooth over the smallest breaks so that (for example) none of the  $\Delta\gamma < 0$  points in Model 5 were apparent. This gives some indication of the observational problems in identifying these features in data on real galaxies. We have confirmed the robustness of the satellite profiles against numerical noise by running a test model with 4X the number of particles (256,000). The resulting profiles and feature measurements show no systematic differences from the 64,000 particle runs.

### 3.5. Dependence on Viewing Angle

Figures 13 and 14 repeat Figures 11 and 12, respectively, for Model 2 viewed at 0, 30, 60 and 90 degrees to its orbital plane (results were similar for all models). Since we are interested in satellites of external galaxies, a single line-of-sight that did not coincide with the view from the center of the parent galaxy (as might have been more appropriate for comparison to Milky Way satellites) was chosen for each viewing angle and held fixed for all orbital phases. The only observable quantities that depend significantly on viewing angle are the ellipse orientation parameters  $\phi$  and  $\gamma_\phi$  — all ellipses align when viewed in the plane of the orbit. In a perfectly spherical parent galaxy, debris particles will stream within the satellite’s orbital plane, so when viewed within that plane there can be no isophote twisting, but simply elongation along the orbit. This will be true close to the satellite even in the case when the parent galaxy is far from spherical since precession of the orbit will only be apparent in debris separated by large orbital phase from the parent.

When we originally performed our analysis we also found that  $\Sigma_{\text{break}}$  and  $\gamma_{\text{xt}}$  were systematically higher when the satellite was viewed from within its orbit. This effect is most pronounced in Model 1, but is somewhat artificial. We repeated the analysis, specifically excluding all particles at distances more than 15 kpc from the satellite along the line of sight, and the differences between the in-plane and out-of-plane views were smaller. We concluded

that our original analysis was contaminated by debris that had stretched entirely around the parent galaxy to intersect the line of sight. Clearly, in the case of Galactic satellites this contamination would only be a problem for satellites within the solar circle. However, it is possible that it could significantly affect in-plane views of satellites around other galaxies.

## 4. Discussion: Derived Quantities

### 4.1. Parameters of Orbit, Orbital Phase and Viewpoint

We begin the discussion with a summary of our findings in the previous section on what surface density maps can tell us about the orbit of the satellite.

#### 4.1.1. Viewpoint

Figures 13 and 14 demonstrate that most observed quantities are not strongly affected by viewing angles greater than 30 degrees from the orbital plane of the satellite. This result is encouraging because it limits the number of parameters that typically need to be considered when interpreting an image. However, the converse of this statement is that it is hard to recover the viewpoint from imaging data alone. The one circumstance that we can clearly interpret in terms of viewpoint is if there is no isophote twisting, then we are viewing a satellite from within its own orbital plane. The aligned isopleths generated from star count data for each of the dwarf spheroidal satellites of our own Milky Way are a prime example of this case (Irwin & Hatzidimitriou 1995).

#### 4.1.2. Orbital Type and Orbital Phase

Our results in preceding sections emphasize that the nature of breaks is both orbit and phase dependent. However, Figures 11 and 12 also suggest a few rules of thumb in interpreting surface brightness distributions.

We found that  $e$ ,  $\gamma_e$  and  $\phi$  are all much lower at the location of a break in the brightness profile caused by heating than one caused by stripping — or, equivalently,  $r_{\text{break}}/r_{\text{distort}} \sim 1$  for a break caused by heating. Such breaks are usually only seen along eccentric orbits and not near the pericentric phases of these orbits. They are accompanied by steep slopes in the surface brightness profiles of the extra-break population. Hence, the combination of a steep slope ( $\gamma_{\text{xt}} < -3$ ) and  $r_{\text{break}}/r_{\text{distort}} \sim 1$  is indicative of a non-circular orbit, with the most



likely inferred orbital eccentricity increasing with the steepness of the slope  $\gamma_{xt}$ .

In contrast,  $r_{\text{break}}/r_{\text{distort}} > 1$  and  $\gamma_{xt} > -3$  both indicate that we are looking at a break where material is being actively stripped. This occurs at any phase along a circular orbit, or near pericenter along a more eccentric orbit.

Note that although it is tempting to use  $\Delta\gamma$  as a diagnostic in the same way as  $\gamma_{xt}$  it would be more difficult to interpret. We expect  $\Delta\gamma$  to depend on the intrinsic profile shape — as reflected in the systematic offset between points in the last two panels of the bottom row of Figure 11, In contrast,  $\gamma_{xt}$  depends predominantly on the fractional variance in the mass loss rate and rate of debris dispersal along an orbit, which we expect to be only loosely dependent on the intrinsic profile shape — as reflected by the much closer agreement between the last two panels of the row above.

We conclude that we can place loose constraints on orbital type and phase using surface brightness data alone.

#### 4.1.3. *Direction of Motion*

Figure 12 shows that though the ellipse orientation and twists tend to point towards the direction of motion along near-circular orbits — i.e.,  $\phi$  and, to a lesser extent,  $\gamma_\phi$  tend to be positive for Models 1–3 — they can be in the opposite sense along more eccentric orbits. Hence determination of the direction of motion from surface brightness data requires some prior constraint on the orbit type or phase.

## 4.2. Relationship of $r_{\text{distort}}$ and $r_{\text{break}}$ to the tidal radius

Since one physical interpretation of  $r_{\text{break}}$  is the point at which the observations become dominated by material leaving the satellite, it is tempting to think of it as analogous to the *tidal radius*  $r_{\text{tide}}$  of the satellite. An estimate of  $r_{\text{tide}}$  for a satellite provides a way of measuring its mass, given that of the parent galaxy (or vice versa) and hence constraining the satellite’s dark matter content (Faber & Lin 1983; Moore 1996; Burkert 1997). Unfortunately, Figure 11 already suggests that  $r_{\text{break}}$  will be a poor indicator of  $r_{\text{tide}}$  — the phase of the orbit where the satellite is most severely tidally limited and  $r_{\text{tide}}$  is smallest is at pericenter, yet there is no signature of a corresponding minimum in  $r_{\text{break}}$ . A possible explanation is that  $r_{\text{break}}$  reflects the tidal limit set at pericenter, as was assumed by King (1962) in his derivation of tidal radii and as seen by Oh & Lin (1992) in their simulations of the disruption of globular clusters.

As a check of this behavior, the top row of panels of Figure 15 shows the ratio of  $r_{\text{break}}$  to the tidal radius set at pericenter,  $r_{\text{tide,peri}}$  (labeled as “ratio 1”), calculated from King’s formula,

$$r_{\text{tide,peri}} = R_{\text{peri}} \left( \frac{m_{\text{sat}}}{M_{\text{gal,peri}}(3 + e_{\text{orb}})} \right)^{1/3} \quad (5)$$

using the known values of the mass of the satellite  $m_{\text{sat}}$ , pericenter of the satellite’s orbit  $R_{\text{peri}}$ , mass of the parent galaxy enclosed within this distance  $M_{\text{gal,peri}}$  and eccentricity of the satellite’s orbit  $e_{\text{orb}}$  for each simulation. (Note: for  $m_{\text{sat}}$  we tried using both the mass enclosed in projection within the  $r_{\text{break}}$  isophote and the mass bound to the satellite from the simulations. We found the latter to be typically 10% larger than the former, which would change  $r_{\text{tide,peri}}$  by only 3%.) The open squares represent  $r_{\text{break}}$  (defined using  $\Delta\gamma_{\text{lim}} = 0.2$  as before), and the crosses are for the analysis repeated, this time requiring  $\Delta\gamma_{\text{lim}} = 1$  (and with a grid extending to  $40 \text{ kpc} \times 40 \text{ kpc}$  for Models 3–5). Recall that along the more eccentric orbits breaks found using  $\Delta\gamma_{\text{lim}} = 0.2$  tended to reflect where the bound portion of the satellite had merely been distorted by the tidal field, while those found using the larger of these limits corresponded to the the point where stripping was actively occurring (see §3.2.1). In all the models,  $r_{\text{break}} > r_{\text{tide,peri}}$  and the open squares hover around  $r_{\text{break}}/r_{\text{tide,peri}} \sim 2$  throughout each orbit, suggesting that this break is indeed in response to a fundamental limit set at pericenter. The open squares and crosses are coincident for Models 1 and 2, but the second set occur at distinctly larger radii in Models 3–5 — a reflection of the separation of the radius where stripping is occurring from where the satellite has actually been distorted by the tidal field, described above.

The second row of panels in Figure 15 show the ratio of  $r_{\text{break}}$  to the instantaneous tidal radius  $r_{\text{tide,inst}}$  (“ratio 2”) for a satellite on a circular orbit at the current distance of the satellite from the parent galaxy  $R$  (i.e. replacing  $R_{\text{peri}}$  with  $R$ ,  $M_{\text{Gal,peri}}$  with  $M_{\text{Gal}}$  and setting  $e_{\text{orb}} = 0$  in equation [5]). The third and fourth row of panels repeat the first and second rows for the ratio of  $r_{\text{distort}}$  to  $r_{\text{tide,peri}}$  (“ratio 3”) and  $r_{\text{tide,inst}}$  (“ratio 4”) . From the second row we can see that the inner and outer breaks straddle  $r_{\text{tide,inst}}$  for much of the orbit for Models 3–5, while the fourth row shows  $r_{\text{distort}} < r_{\text{tide,inst}}$  for each model and throughout each orbit. These characteristics emphasize that it can be possible to see elongations, twists and break radii well within the point where one might expect tidal effects to be important (e.g. by calculating  $r_{\text{tide,inst}}$  using dynamical estimates for  $M_{\text{gal}}$  and  $m_{\text{sat}}$ ).

We have already concluded that  $r_{\text{break}}/r_{\text{distort}}$  can place weak constraints on the orbit type and phase, and indicate whether a break is due to heating or stripping processes. Figure 16 shows  $r_{\text{break}}/r_{\text{tide}}$  and  $r_{\text{distort}}/r_{\text{tide}}$ , calculated using both pericentric and instantaneous values of  $r_{\text{tide}}$ , as a function of  $r_{\text{break}}/r_{\text{distort}}$ . It is intended to illustrate the extent to which the observables  $r_{\text{break}}$  and  $r_{\text{distort}}$  might be used to constrain  $r_{\text{tide,inst}}$  and  $r_{\text{tide,peri}}$ . We find:

(i) if  $r_{\text{break}}/r_{\text{distort}} \sim 1$  then  $r_{\text{tide,peri}} < r_{\text{break}} < 2r_{\text{tide,peri}}$  and we expect to be at a phase where  $r_{\text{tide,inst}} > r_{\text{tide,peri}}$ ; and (ii) if  $r_{\text{break}}/r_{\text{distort}} > 2$  then  $0.5r_{\text{tide,peri}} < r_{\text{distort}} < 1.5r_{\text{tide,peri}}$  and  $r_{\text{tide,inst}} < r_{\text{break}} < 2r_{\text{tide,inst}}$ . Unfortunately, such arguments can at best lead to an estimate of the tidal radius that is good to within a factor of two. In these circumstances it is dangerous to use our estimated  $r_{\text{tide}}$  in equation (5) to estimate the mass of either the parent or satellite galaxy since this order unity error in  $r_{\text{tide}}$  would lead to an order of magnitude error in the mass estimate. Indeed, it may be possible to reconcile the small cutoff radii observed when deriving surface density profiles of the Milky Way’s dwarf spheroidal satellites from star-counts (Irwin & Hatzidimitriou 1995) with the large dark matter content implied by their velocity dispersions by assuming these satellites are near the apocenters of their highly-eccentric orbits. Such a conjecture needs to be tested more thoroughly with models specifically designed to mimic the observed properties of these galaxies.

### 4.3. Mass Loss Rates

In their interpretation of debris populations, Johnston, Sigurdsson & Hernquist (1999) derived an expression for the surface density of the extra-break population by assuming that once material is unbound from a satellite it is not influenced significantly by the satellite’s gravitational field and by arguing that debris material will spread away from a satellite at the characteristic rate  $\pi r_{\text{break}}/T_{\text{orb}}$ . They found

$$\Sigma_{\text{xt}}(r) = \frac{dm}{dt} \frac{T_{\text{orb}}}{\pi} \frac{1}{2\pi r_{\text{break}} r} \quad (6)$$

where  $T_{\text{orb}}$  is the azimuthal time period of the satellite’s orbit (time taken to cover  $2\pi$  in angle along the orbit) and  $dm/dt$  is the mass loss rate from the satellite. By overlaying this expression on the surface density profiles in the simulations they demonstrated that it compared well for satellites on near-circular orbits, and concluded that outlying populations with slopes of  $\gamma = -1$  are likely to be explained as tidal debris. By contrast, note that  $\gamma$  was typically less than  $-1$  in all our simulations (Figures 11 and 13), and in those of Combes, Leon & Meylan (1999).

The apparent contradiction between our simulations and equation (6) can be resolved by noting that: (i) close to the satellite we do expect debris particles to still be influenced to some extent by tidal forces (in contrast to the assumption in the previous paragraph) — in Figure 5 the particles are seen to move perpendicular to the satellite’s orbit (i.e., in the direction of tidal forces) before being stretched along it; (ii) both the mass loss rate and the rate of debris dispersal are phase-dependent along eccentric orbits; (iii) breaks can occur well within the still-bound population of the satellite.

An alternative expression for the surface density that captures some of the above behavior is

$$\Sigma_{\text{xt}}(r) \propto \frac{dm}{dt} \frac{T_{\text{circ}}}{r^2} \quad (7)$$

where the drift rate is now assumed to increase with  $r$  and the variable rate of debris dispersal along the orbit has been represented by replacing  $T_{\text{orb}}$  with the time period for a circular orbit at the satellite’s instantaneous position,  $T_{\text{circ}}$ . In fact, throughout Model 1 (the near-circular case) the slope hovered in the range  $-3 < \gamma_{\text{xt}} < -1$ , suggesting that the true behavior lies somewhere between the simplified representations given in equations (6) and (7) as debris stars are observed in transition between being bound and unbound. This effect was not noted by Johnston, Sigurdsson & Hernquist (1999) because they did not explicitly fit slopes to their extra-tidal populations but rather overlaid models on the surface density profiles. Also, they did not consider eccentric orbits where the variance in slopes is even more pronounced and only examined their simulations at a limited number of orbital phases. (Note that neither approach takes into account the variable mass loss rate along the orbit which would also affect  $\gamma_{\text{xt}}$  and could explain the more extreme  $\gamma_{\text{xt}} < -2$  cases not consistent with either equation.)

Johnston, Sigurdsson & Hernquist (1999) re-arranged equation (6) to estimate the mass loss rate from a satellite using observed quantities, and found that, when applied to simulations of satellites on near-circular orbits, this approach could be used to reproduce the mass loss rate in the simulation to within a factor of two. In Figure 17 we re-examine the accuracy of this approach at all phases of the more eccentric orbits studied in this paper, using equation (7) evaluated at  $r_{\text{break}}$ . We first find the “best” constant of proportionality for this equation to be  $5/(4\pi^2)$  by requiring the estimate to closely match the known mass loss rate in the simulation throughout Model 1 (where the  $\pi^2$  is used instead of a numerical value to mimic equation [6]). We then use this value for our estimates along the more eccentric orbits. The solid line represents the mass loss rate in the simulation (averaged over one tenth of the orbit) and the symbols are the “observed” mass loss rate estimated at  $r_{\text{break}}$ , defined as usual with  $\Delta\gamma_{\text{lim}} = 0.2$  (open squares), and at  $r_{\text{break}}$  defined with  $\Delta\gamma_{\text{lim}} = 1.0$  (crosses). The mass loss estimate derived from observable quantities reproduces the approximate amplitude as a function of phase along Models 1–3. It is less successful along the most eccentric orbit, in particular where we know the break to be within the bound satellite population and do not expect the debris to be dispersing freely.

Note that this idea can be extended once longer portions of a satellite’s debris stream are available to reconstruct a detailed mass loss history from breaks between populations lost on different orbits or different disk passages (see Combes, Leon & Meylan, 1999 and Leon, Meylan & Combes, 2000; also Johnston et al., 1999, for a discussion of this idea in the

context of the Sagittarius dwarf spheroidal galaxy).

## 5. Summary

In this paper we have attempted to understand how the morphology of faint populations around satellite galaxies might be interpreted in terms of the orbit and orbital phase of the satellite, and the tidal influence of the parent galaxy. We have found that breaks in the surface density profile can be signatures of heating within the bound satellite population, stripping of debris from the satellite, or the transition between distinct debris populations. Multiple breaks can be found within a single satellite profile and attributed to one or more of these effects. Breaks can be above or below the inner profile of the satellite and the surface density of extra-break material can have widely varying amplitude and slopes (we found  $-5 < \gamma_{\text{xt}} < -1$ ). Morphological distortions to the satellite in the form of increasing ellipticity and twisting of isophotes can occur well within any identified break radii. The identification of break radii depends on the choice of  $\Delta\gamma_{\text{lim}}$ , inner satellite profile and resolution of observations.

Using surface brightness distributions alone we expect to be able place loose constraints on either the precentric or instantaneous tidal radius, mass loss rate, orbital type and phase of the satellite and nature of breaks in the surface brightness profile. For example, we have found that breaks well within the bound satellite population tend to only occur along the more eccentric orbits at phases when the satellite is not near pericenter. Such breaks are usually coincident with the onset of other morphological disturbances such as increasing isophote ellipticity or twisting (or  $r_{\text{break}} \sim r_{\text{distort}}$ ). By contrast, along circular orbits and near pericenter of eccentric orbits breaks tend only to be identified at radii much greater than where disturbances in the morphology first become apparent (or  $r_{\text{break}} > r_{\text{distort}}$  — note that this can also occur at apocenter along eccentric orbits if the inner break is too subtle to be detected) and usually indicate the region where material is being actively stripped from the satellite. Hence a satellite with  $r_{\text{break}} \sim r_{\text{distort}}$  is likely to be on an eccentric orbit and have an instantaneous tidal radius much larger than  $r_{\text{break}}$ . One with  $r_{\text{break}} > r_{\text{distort}}$  could be at any phase of a circular or eccentric orbit, with the break corresponding to the transition between bound and unbound material. Our results are largely independent of viewpoint, as long as we are not viewing the satellite directly within its orbital plane.

We conclude that though surface brightness distributions contain a wealth of information, degeneracies in orbital type and orbital phase dependencies limit the extent to which they can be interpreted physically. In a further paper we look at what more might be gained by using photometric data in conjunction with spectroscopic data.

We thank the referee for her/his many detailed and insightful comments. KVVJ acknowledges support in part as a member of the Institute for Advanced Study, and from NASA LTSA grant NAG5-9064. PIC thanks the ARCS foundation and the NSF for support as an ARCS Foundation scholar and an NSF graduate student research fellow.

## REFERENCES

- Binney, J. & Tremaine, S. 1987, *Galactic Dynamics* (Princeton: Princeton University Press)
- Burkert, A. 1997, *ApJ*, 474, L99
- Choi, P. I., Guhathakurta, P. & Johnston, K. V. 2002, *AJ*, submitted
- Combes, F., Leon, S. & Meylan, G. 1999, *A&A*, 352, 149
- Faber, S. M. & Lin, D. N. C. 1983, *ApJ*, 266, L17
- Ghigna, S., Moore, B., Governato, F., Lake, G., Quinn, T., & Stadel, J. 1998, *MNRAS*, 300, 146
- Gould, A., Guhathakurta, P. Richstone, D. & Flynn, C. 1992, *ApJ*, 388, 354
- Grillmair, C. J. 1998, in *Galactic Halos*, ed. D. Zaritsky (ASP Conf. Ser., Vol. 136), p. 45
- Grillmair, C. J., Lauer, T. R., Worthey, G., Faber, S. M., Freedman, W. L., Madore, B. F., Ajhar, E. A., Baum, W. A., Holtzman, J. A., Lynds, C. R., O’Neil, E. J., Jr. & Stetson, P. B. 1996, *AJ*, 112, 1975
- Grillmair, C. J., Freeman, K. C., Irwin, M. & Quinn, P. J. 1995, *AJ*, 109, 2553
- Guhathakurta, P., Choi, P. I. & Raychaudhury, S. 2002, *AJ*, in prep
- Helmi, A. & White, S. D. M. 1999, *MNRAS*, 307, 495
- Hernquist, L. 1990, *ApJ*, 356, 359
- Hernquist, L. & Ostriker, J. P. 1992, *ApJ*, 386, 375
- Hodge, P. W. 1973
- Irwin, M. J. & Hatzidimitriou, D. 1995, *MNRAS*, 277, 1354
- Johnston, K. V. 1998, *ApJ*, 495, 297

- Johnston, K. V., Majewski, S. R., Siegel, M. H., Kunkel, W. E. & Reid, I. N. 1999, *AJ*, 118, 1719
- Johnston, K. V., Hernquist, L. & Bolte, M. 1996, *ApJ*, 465, 278
- Johnston, K. V., Sigurdsson, S & Hernquist, L. 1999, *MNRAS*, 302, 771
- Kent, S. M. 1987, *AJ*, 94, 306
- King, I. R. 1962, *AJ*, 67, 471
- Klessen, R. S. & Kroupa, P. 1998, *ApJ*, 498, 143
- Kuhn, J. R. 1993, *ApJ*, 409, L13
- Kuhn, J. R. & Miller, R. H. 1989, *ApJ*, 341, L41
- Kuhn, J. R., Smith, H. A. & Hawley, S. L. 1996, *ApJ*, 469, L93
- Leon, S., Meylan, G. & Combes, F. 2000, *A&A*, 359, 907
- Majewski, S. R., Ostheimer, J. C., Patterson, R. J., Kunkel, W. E., Johnston, K. V. & Geisler, D. 2000, *AJ*, 119, 760
- Mateo, M., Olszewski, E. W. & Morrison, H. L. 1998, *ApJ*, 508, L55
- Miyamoto, M. & Nagai, R. 1975, *PASJ*, 27, 533
- Moore, B. 1996, *ApJ*, 461, L13
- Odenkirchen, M., et al. 2000, *astro-ph/0012311*
- Oh, K. S. & Lin, D. N. C. 1992, *ApJ*, 386, 519
- Quinn, P. J. 1984, *ApJ*, 279, 596
- Toomre, A. & Toomre, J. 1972, *ApJ*, 178, 623
- Tormen, G., Bouchet, F. R., & White, S. D. M. 1997, *MNRAS*, 286, 865
- Tremaine, S. 1993, in *Back to the Galaxy*, eds. S. S. Holt & F. Verter (New York: AIP), p. 599
- Weinberg, M. D. 1994, *AJ*, 108, 1398
- Weinberg, M. D. 1994, *AJ*, 108, 1414

Weinberg, M. D. 1994, AJ, 108, 1403



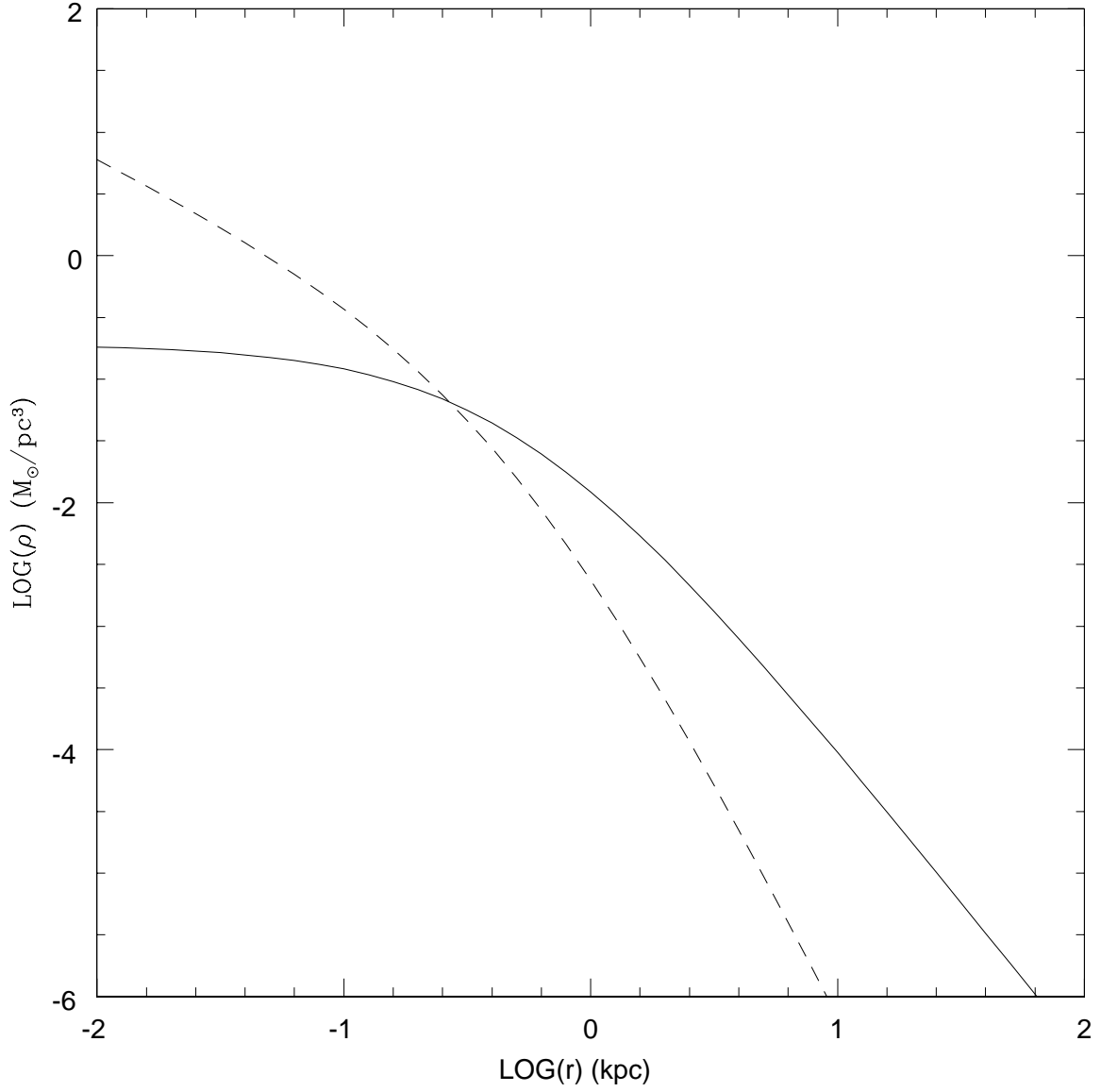


Fig. 1.— Plummer (solid line) and Hernquist (dashed line) density profiles of satellites used in the simulations.

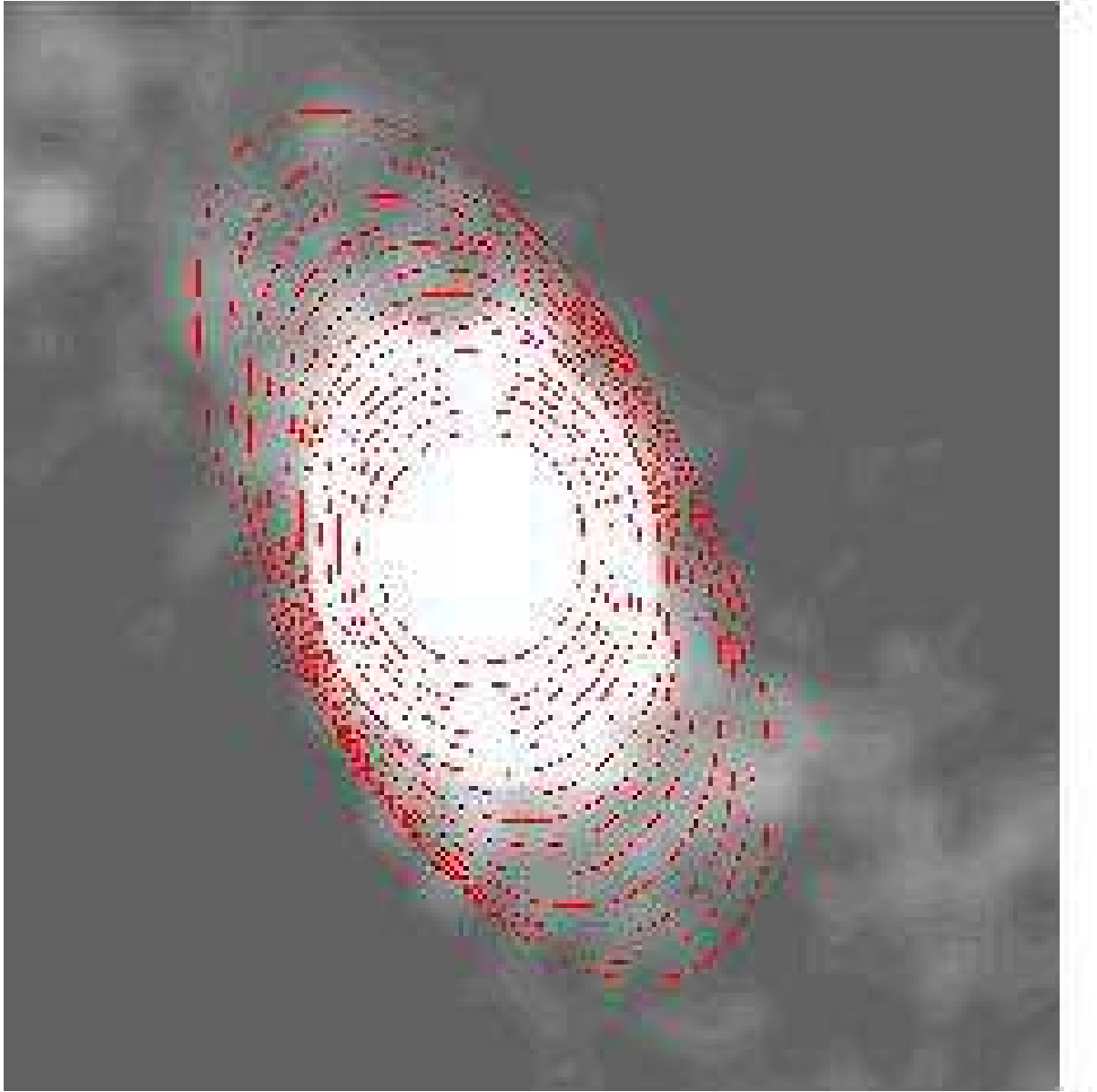


Fig. 2.— Grayscale image of particle density in Snapshot 121 from Model 1, overlaid with

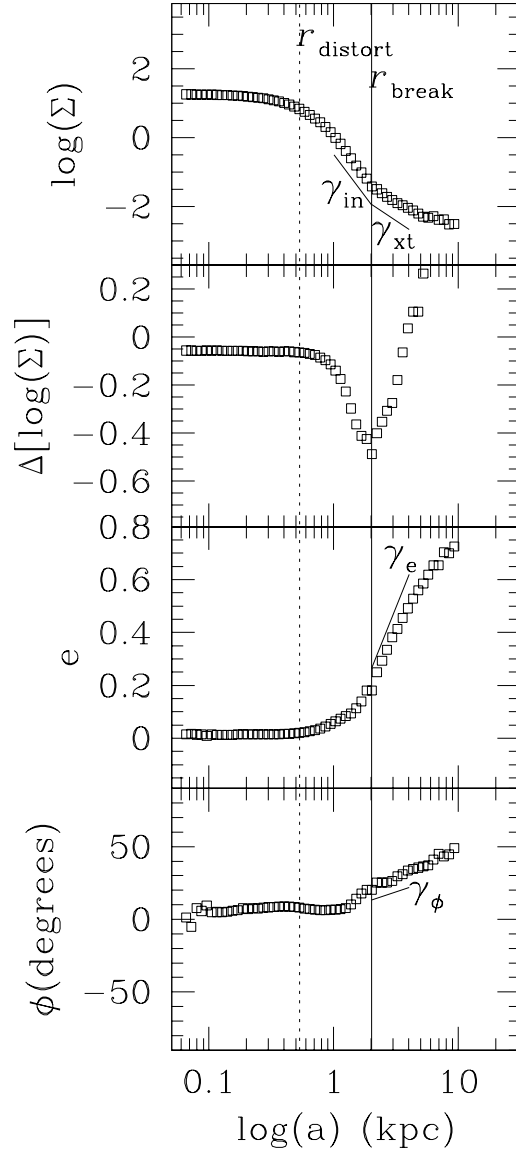


Fig. 3.— The open squares in each panel illustrate the results of isophotal analysis (ellipse fits) of Snapshot 121 from Model 1 (top to bottom): surface density (brightness) profile; difference between instantaneous and initial brightness profiles; ellipticity; and position angle, measured from the satellite-parent galaxy line towards the satellite’s projected direction of motion. The dotted line running through each panel indicate the position of  $a = r^{\text{distort}}$  and the solid line shows  $a = r^{\text{break}}$  (see text for explanation). The short solid lines indicate the slopes in each quantity fitted to points lying within a factor of two of  $r^{\text{break}}$ .

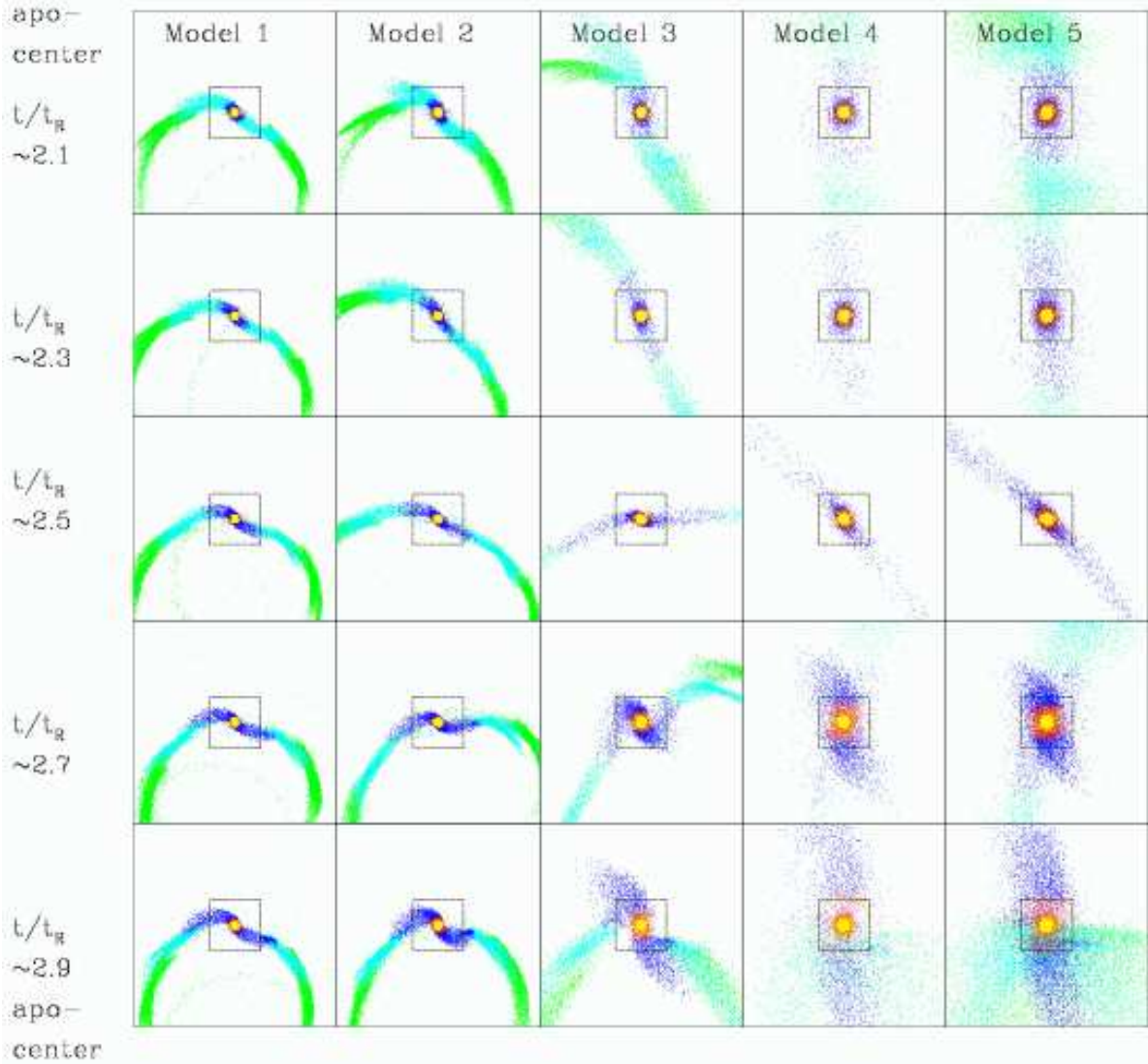


Fig. 4.— Projection of “debris” particles onto the orbital plane for snapshots equally spaced along in time along third radial orbit of each orbit. The green/cyan/blue/red/yellow particles are (were/will be) lost during orbits 1/2/3/4/5 according to the energy criterion described in §3.1 (those not lost during the simulation are not shown). The parent galaxy is on the negative  $Y$ -axis in all panels, and the box size is  $80 \text{ kpc} \times 80 \text{ kpc}$ .

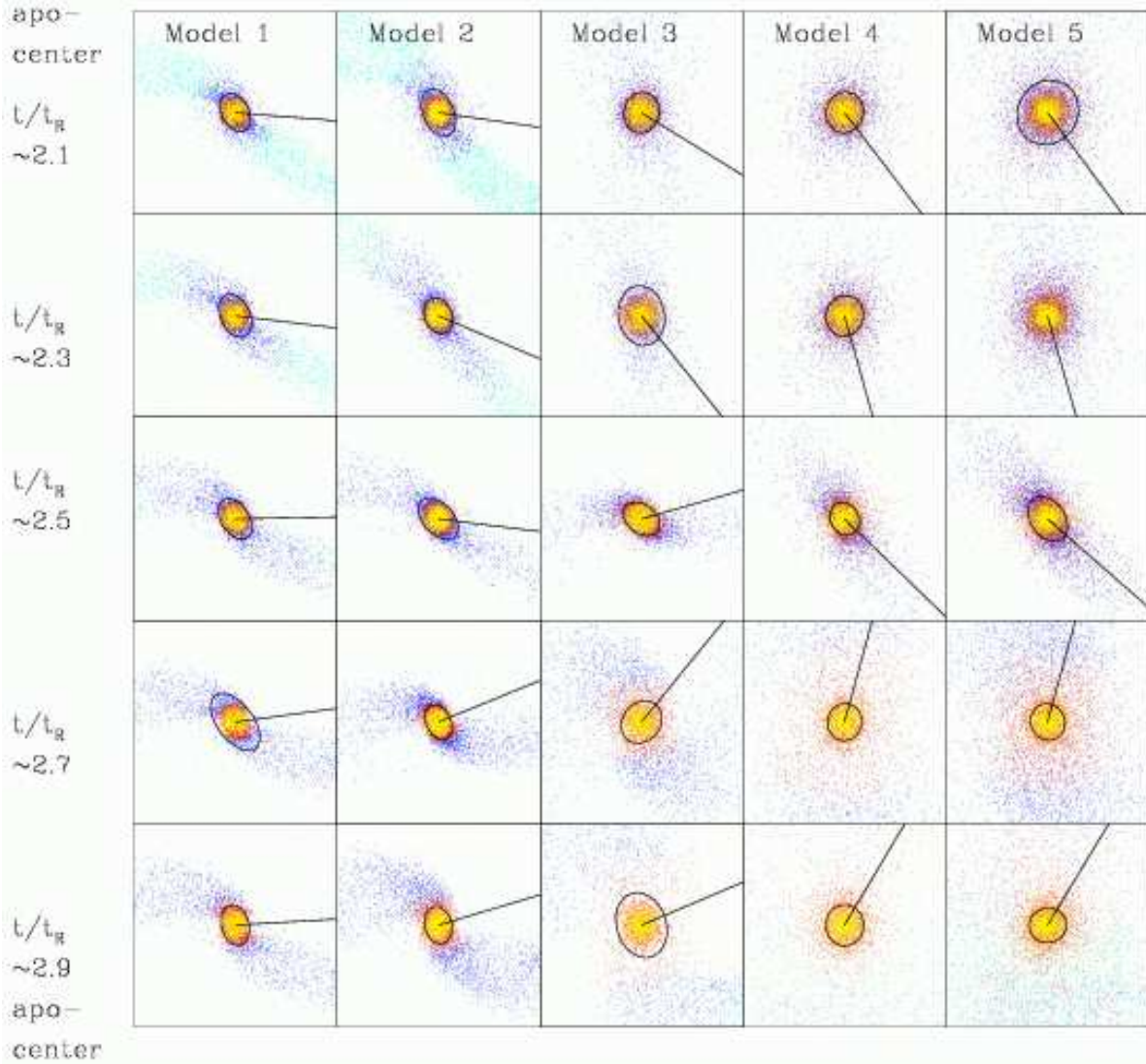


Fig. 5.— As Figure 4, but for a box size of  $20 \text{ kpc} \times 20 \text{ kpc}$ . The ellipse corresponds to the isophote at  $r_{\text{break}}$ , the innermost break radius identified using  $\Delta\gamma_{\text{lim}} = 0.2$  in each case, and the line indicates the velocity vector of the satellite.

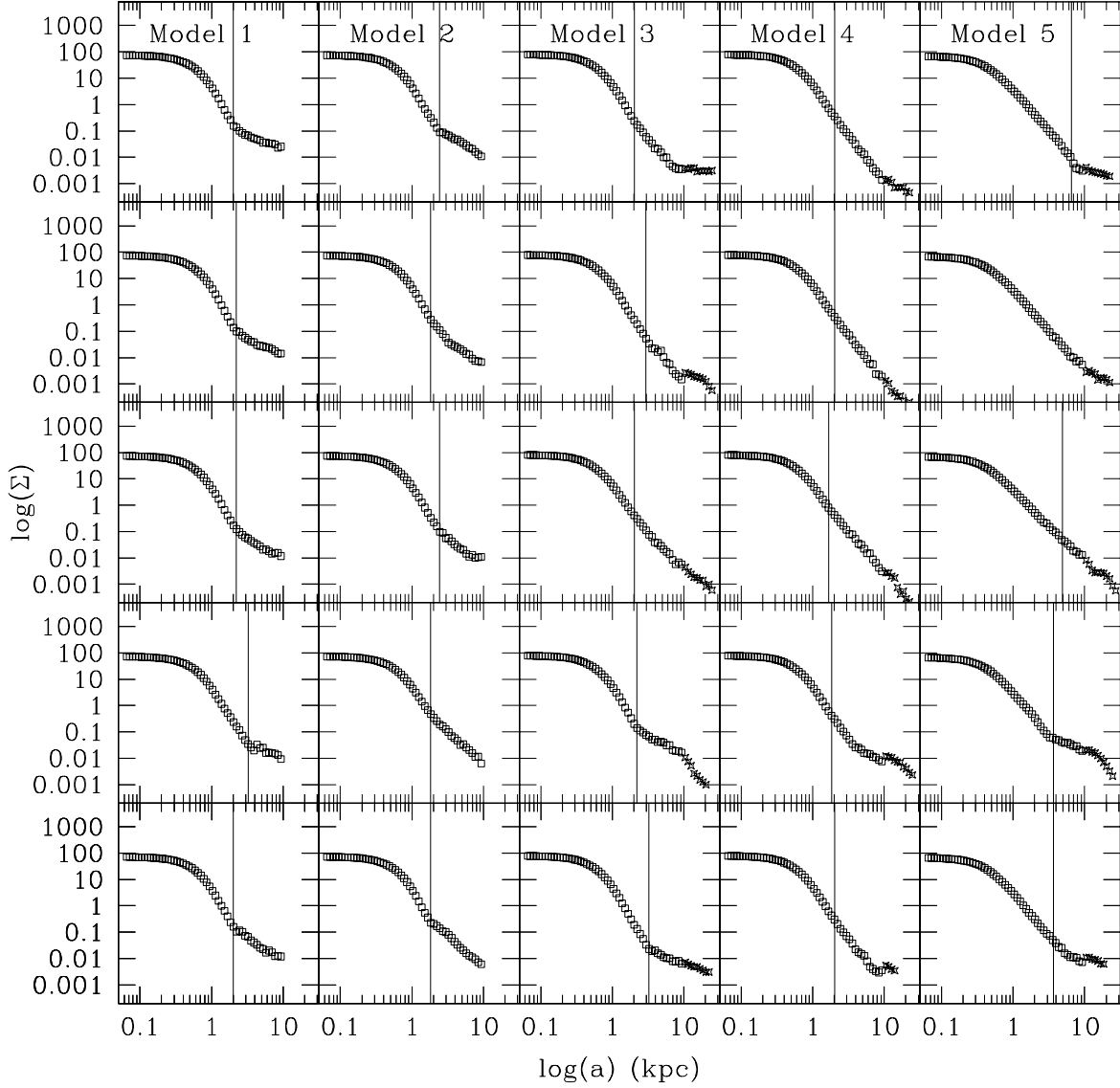


Fig. 6.— Surface density profiles corresponding to each of the panels in Figure 5. The open squares are from the analysis on the  $20\text{kpc}\times 20\text{kpc}$  box and the stars are for the analysis on the  $40\text{kpc}\times 40\text{kpc}$  box. The solid line indicates the location of  $r_{\text{break}}$ . No line is included in the second panel of Model 5 because no break was found in this case.

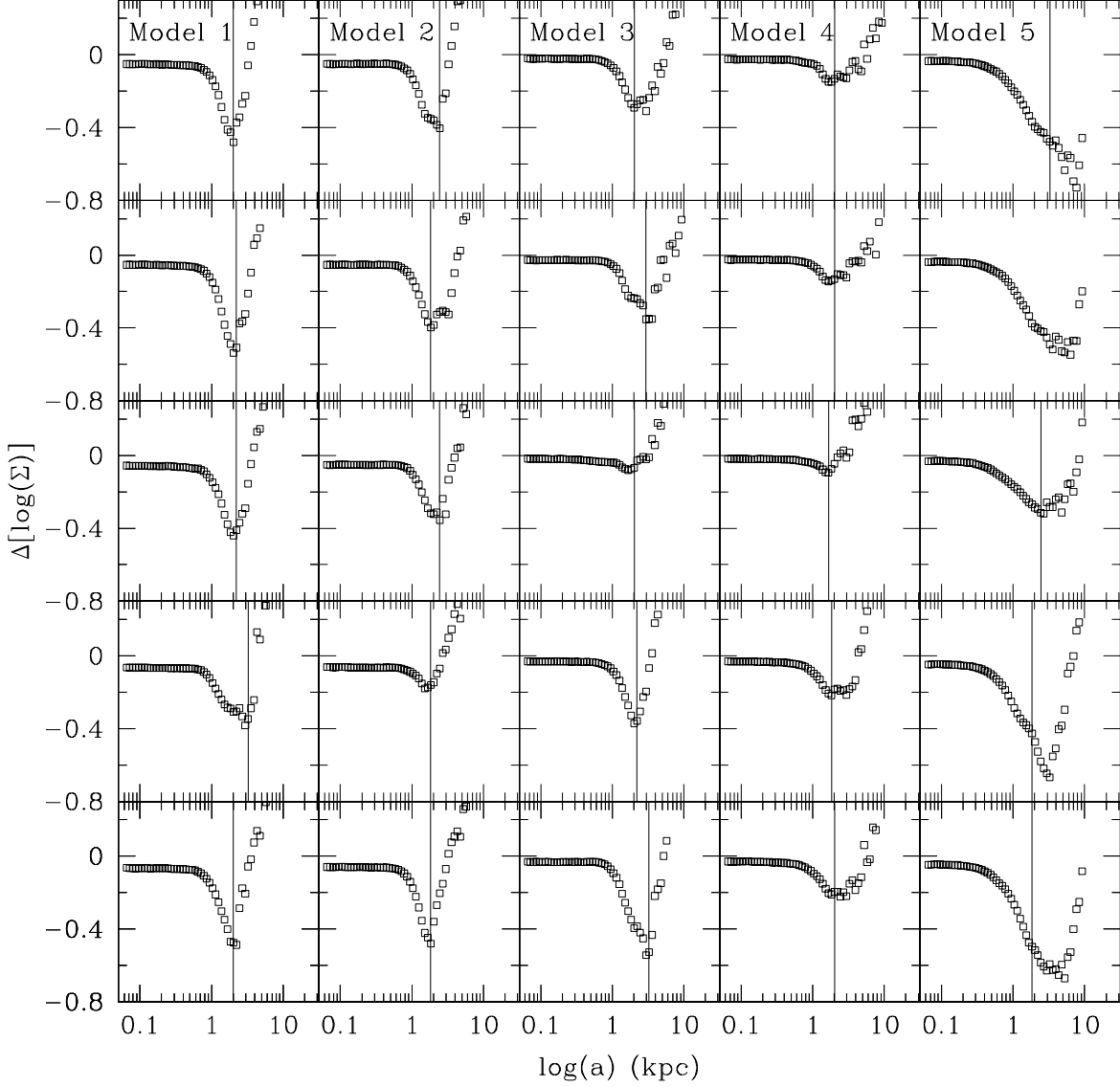


Fig. 7.— The difference between the current and initial surface density profile of the satellite corresponding to each of the panels in Figure 5. The solid line indicates the location of  $r_{\text{break}}$ .

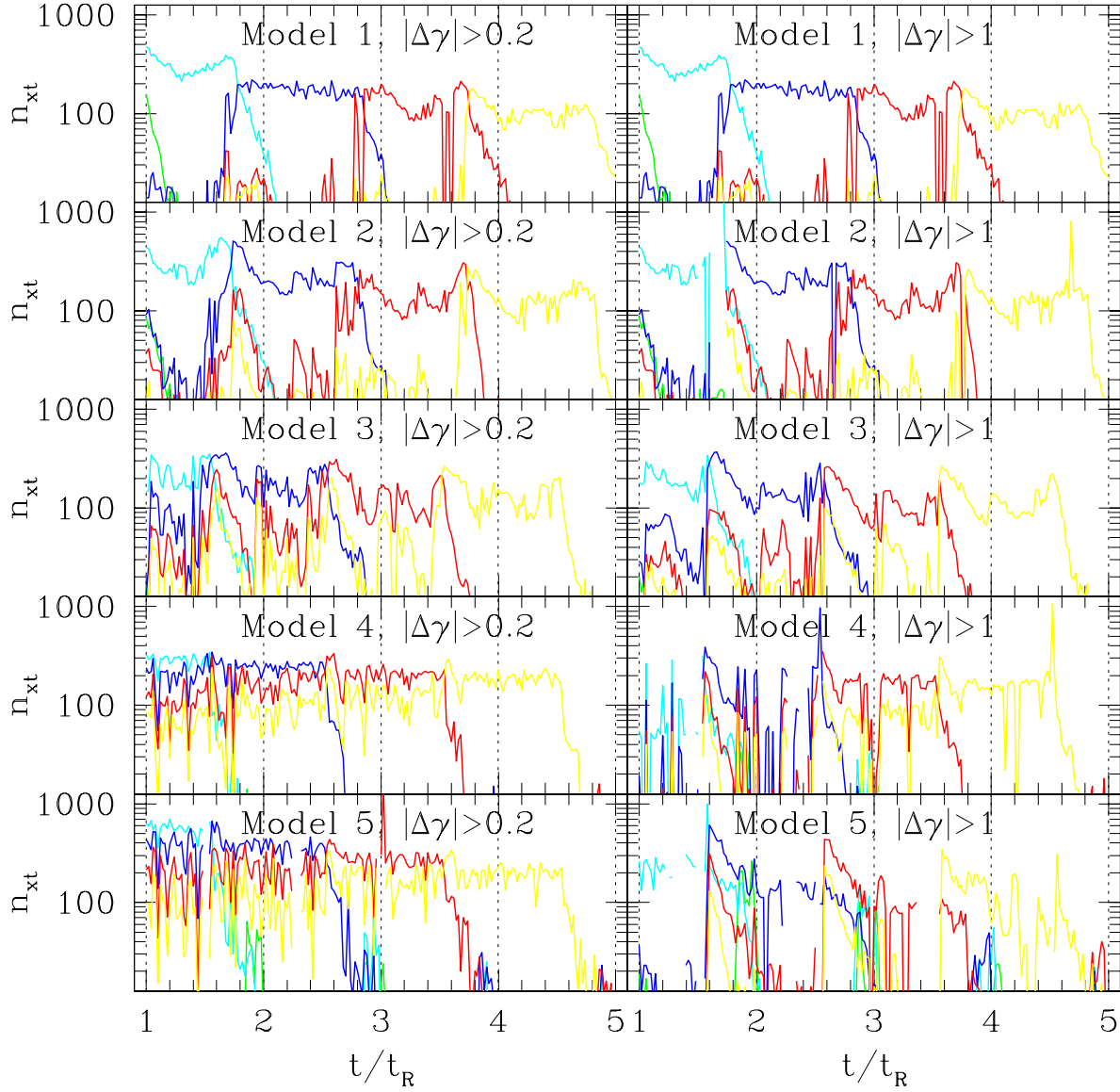


Fig. 8.— The number of particles found in the region  $0.9r_{\text{break}} < a < 1.1r_{\text{break}}$  from each of the debris populations (color coded as Figures 4 and 5) for  $\Delta\gamma_{\text{lim}} = 0.2$  (left hand panels) and  $\Delta\gamma_{\text{lim}} = 1.0$  (right hand panels).



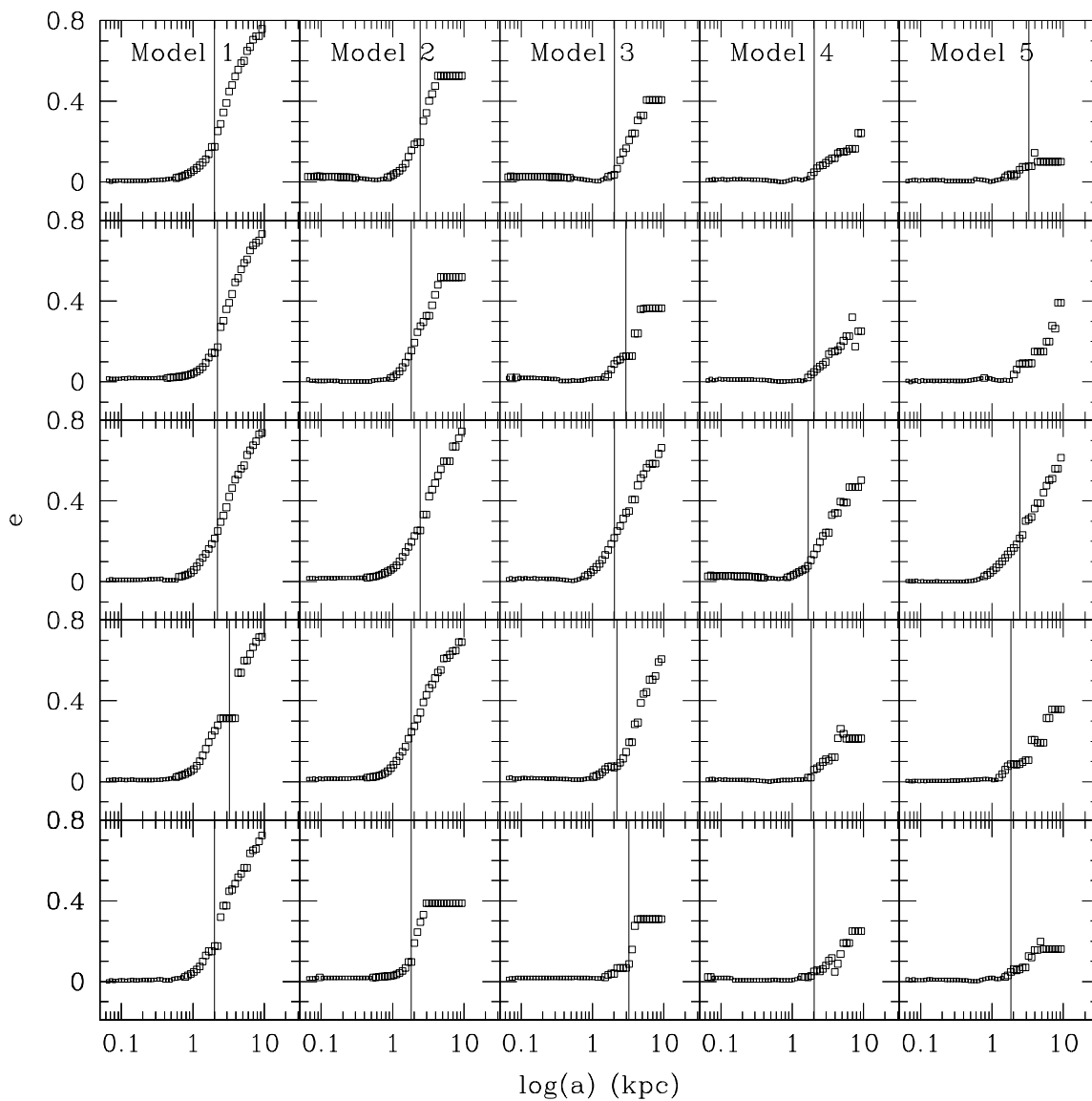


Fig. 9.— Ellipticity profiles corresponding to each of the panels in Figure 5. Miniature squares are plotted if  $e < 0.02$ . The solid line indicates the location of  $r_{\text{break}}$ .

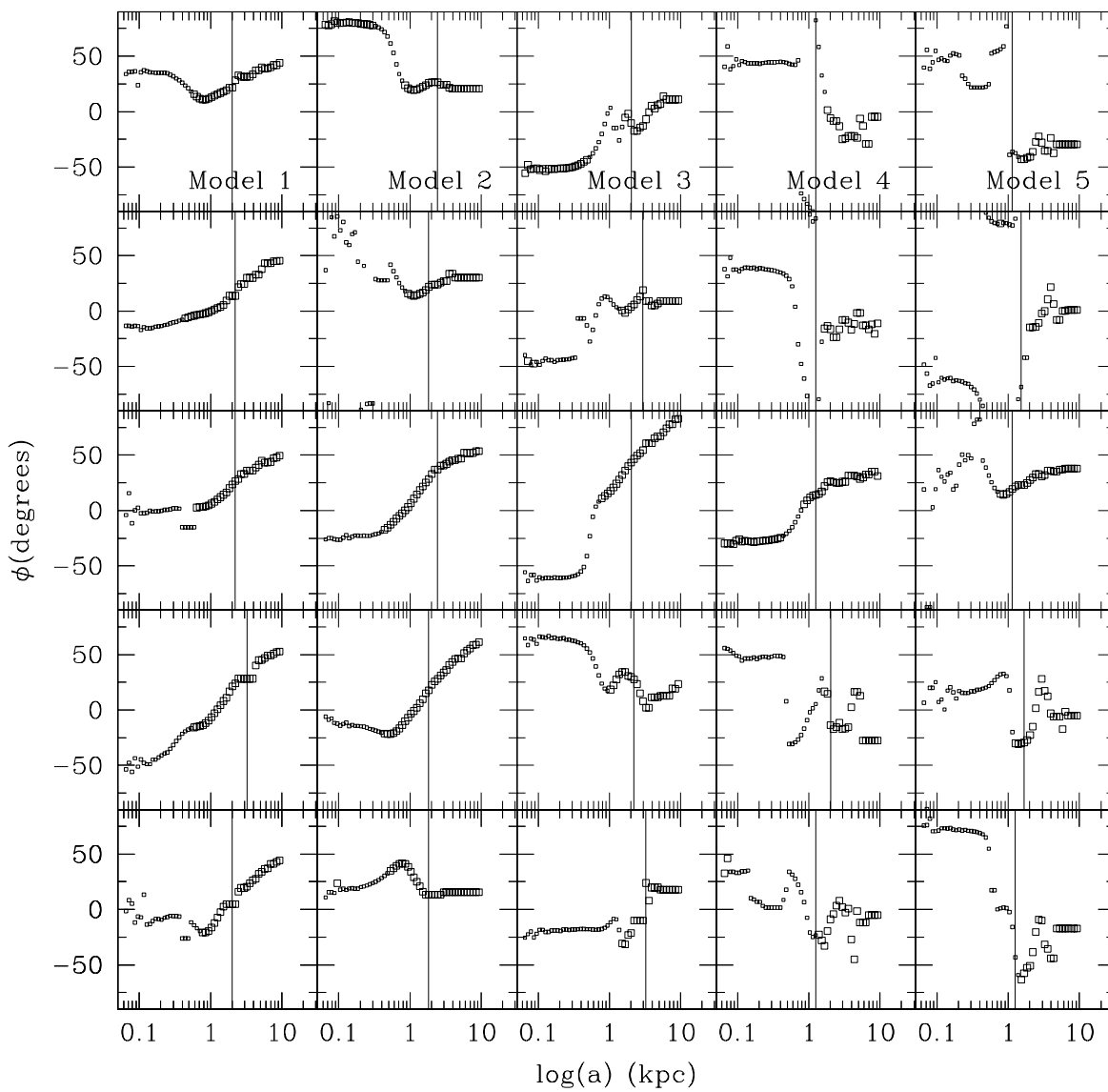


Fig. 10.— Position angle profiles corresponding to each of the panels in Figure 5. Mini-squares are plotted if  $e < 0.02$ . The solid line indicates the location of  $r_{\text{break}}$ .

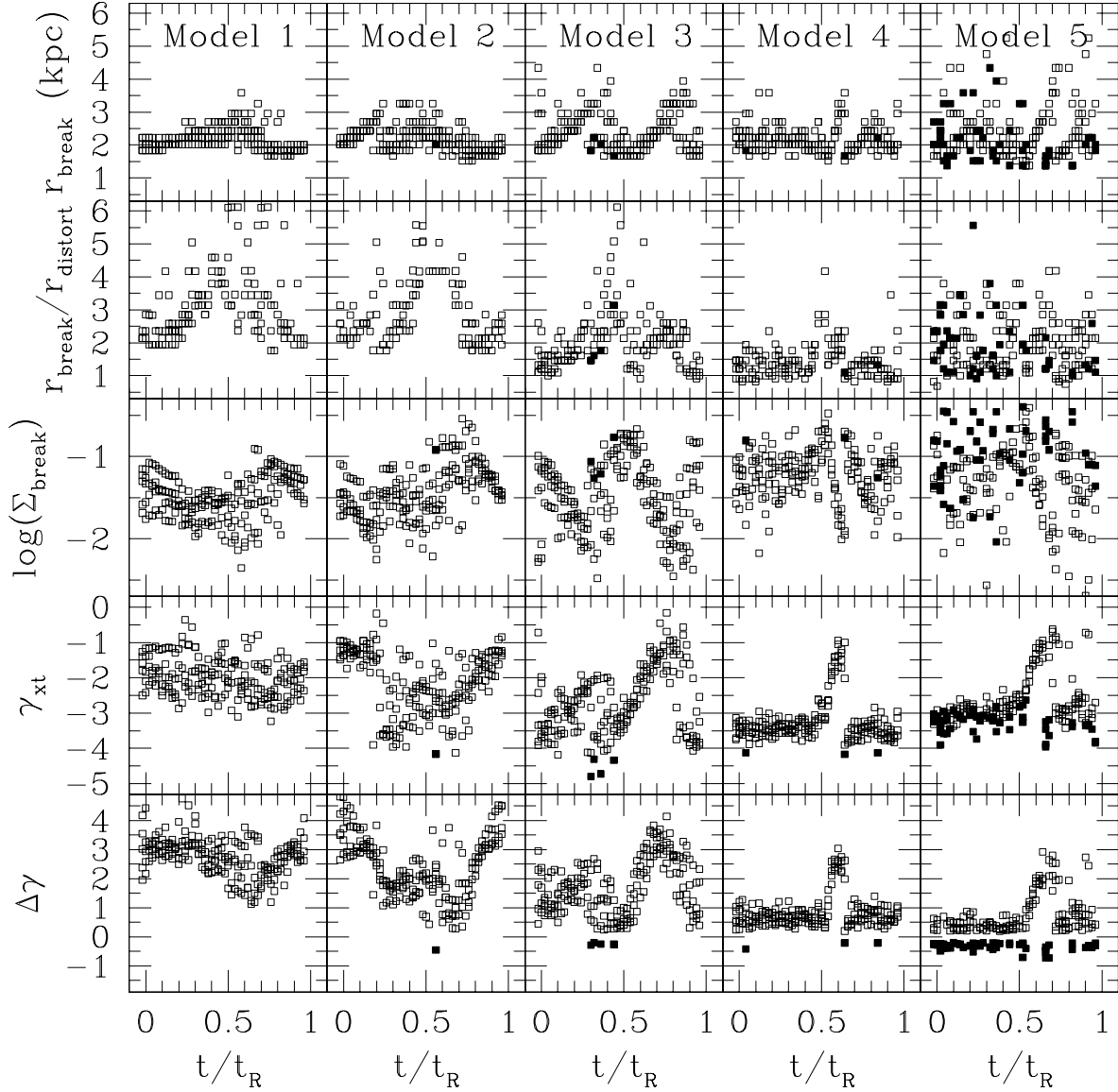


Fig. 11.— Summary of “observed” quantities derived from the surface density profiles of all 250 snapshots of each model as a function of orbital phase (top to bottom): radius at which the first significant break occurs in the brightness profile; ratio of  $r_{\text{break}}$  to the radius at which the isophotes start becoming significantly distorted; surface brightness at  $r_{\text{break}}$ ; slope of brightness profile beyond  $r_{\text{break}}$ ; and change in slope of the brightness profile at  $r_{\text{break}}$ . Apocenter is at  $t/t_R = 0$  and 1, pericenter is at  $t/t_R = 0.5$ . The solid squares highlight points where  $\Delta\gamma < 0$ .

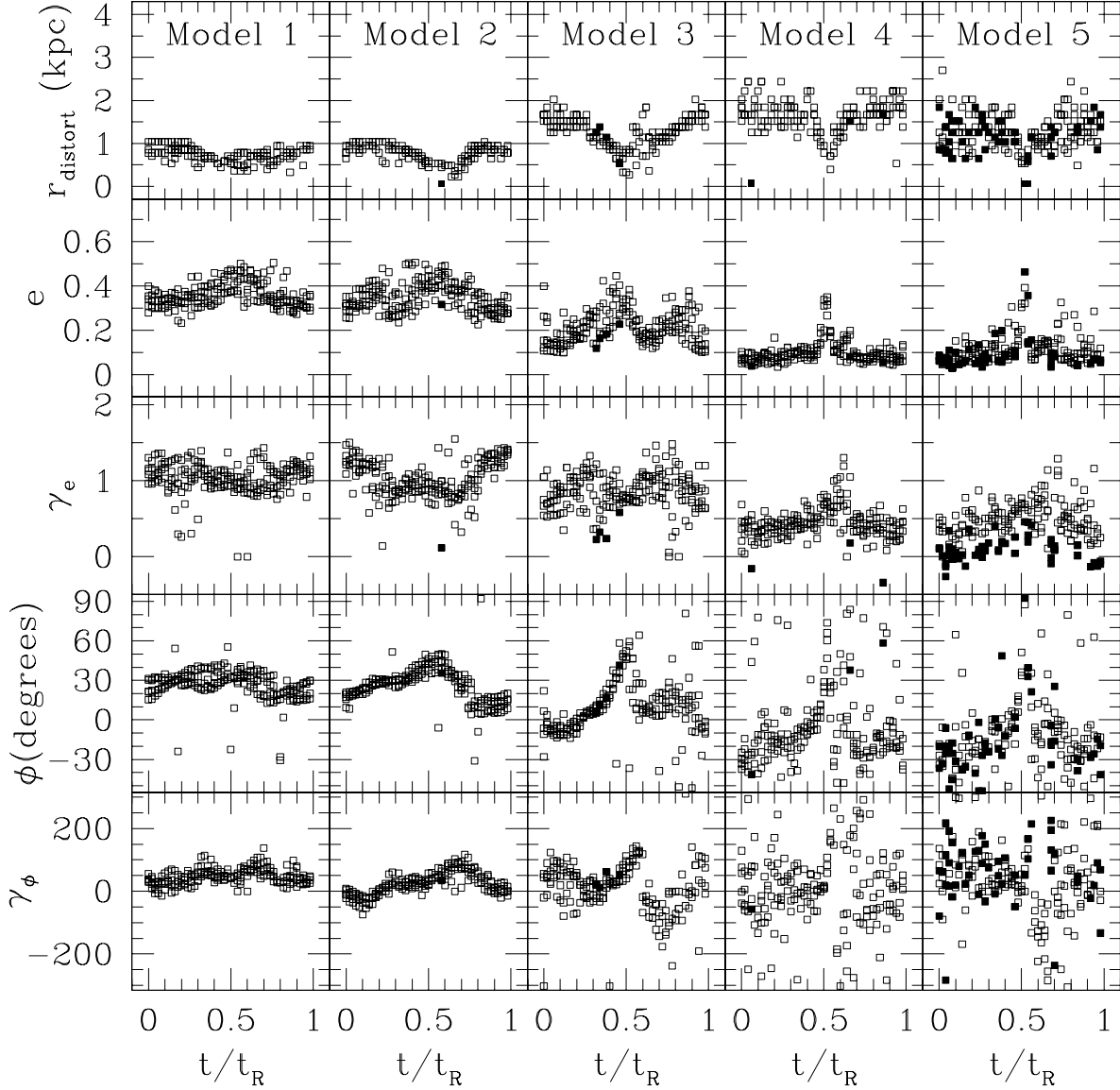


Fig. 12.— Summary of “observed” quantities from the isophotal shapes of all 250 snapshots of each model as a function of orbital phase (top to bottom): radius at which the isophotes start becoming significantly distorted; ellipticity at  $r_{\text{break}}$ ; rate of change of ellipticity with radius beyond  $r_{\text{break}}$ ; position angle at  $r_{\text{break}}$ ; and rate of change of position angle with radius beyond  $r_{\text{break}}$ . Apocenter is at  $t/t_R = 0$  and 1, pericenter is at  $t/t_R = 0.5$ . The solid squares highlight points where  $\Delta\gamma < 0$ .

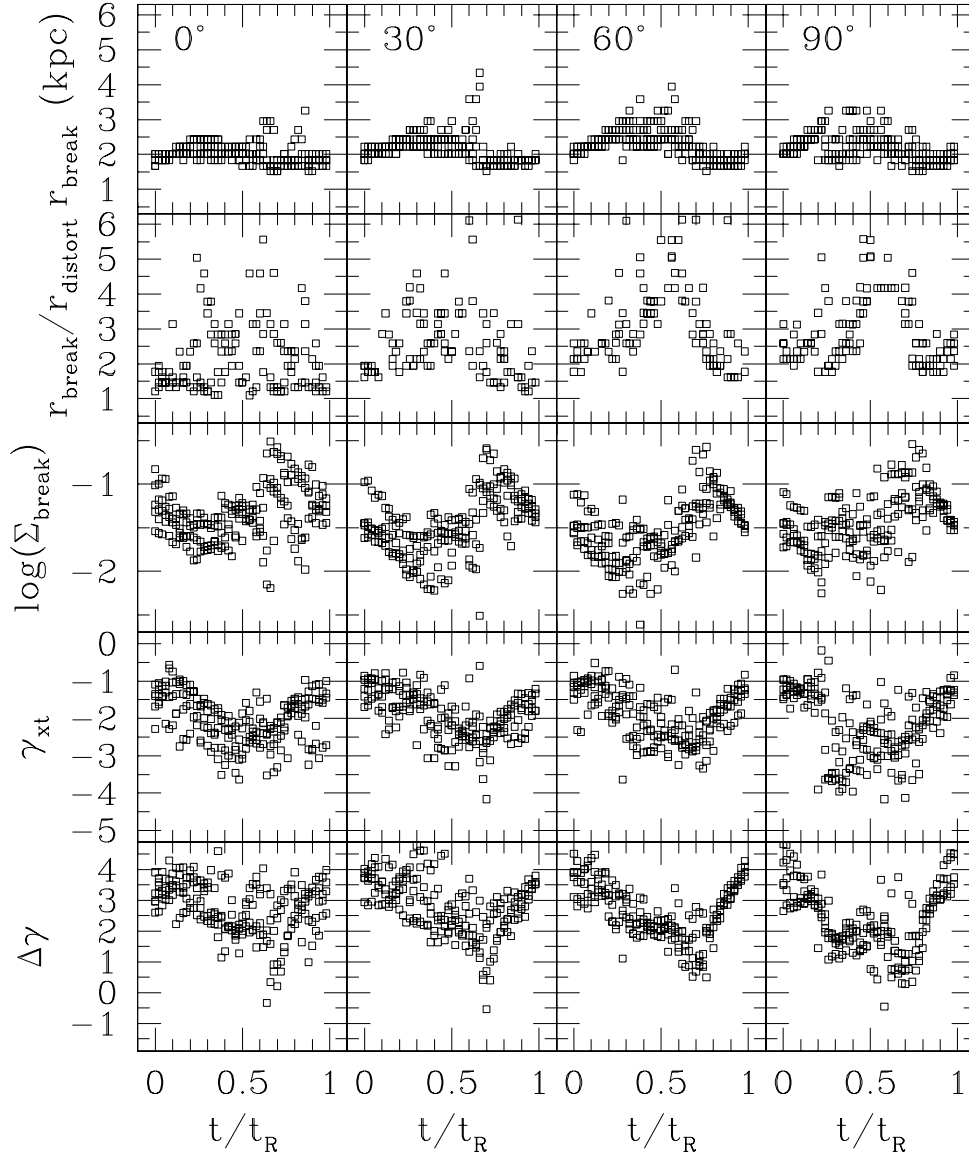


Fig. 13.— Repeat of Figure 11 for Model 2 viewed at 0, 30, 60 and 90 degrees to the orbital plane.

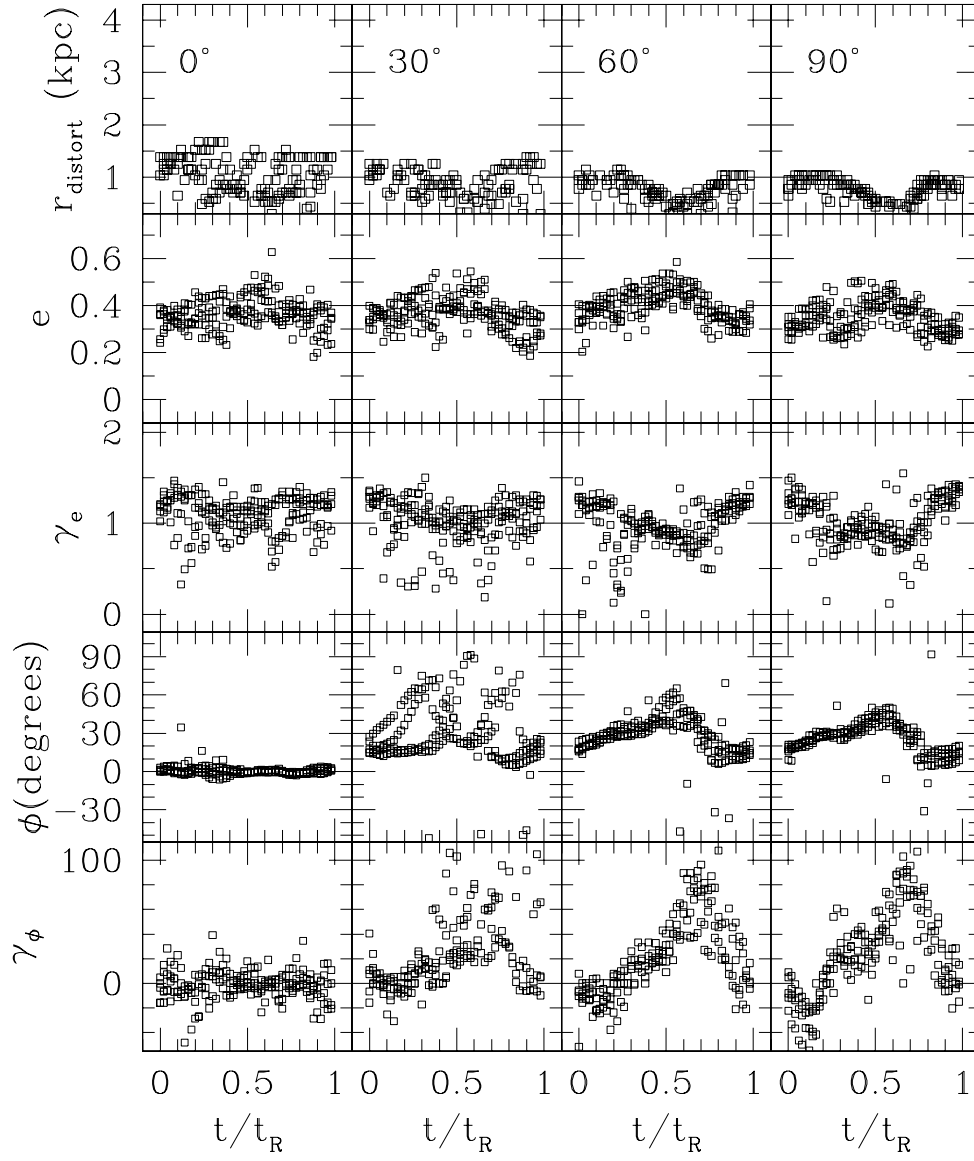


Fig. 14.— Repeat of Figure 12 for Model 2 viewed at 0, 30, 60 and 90 degrees to the orbital plane.

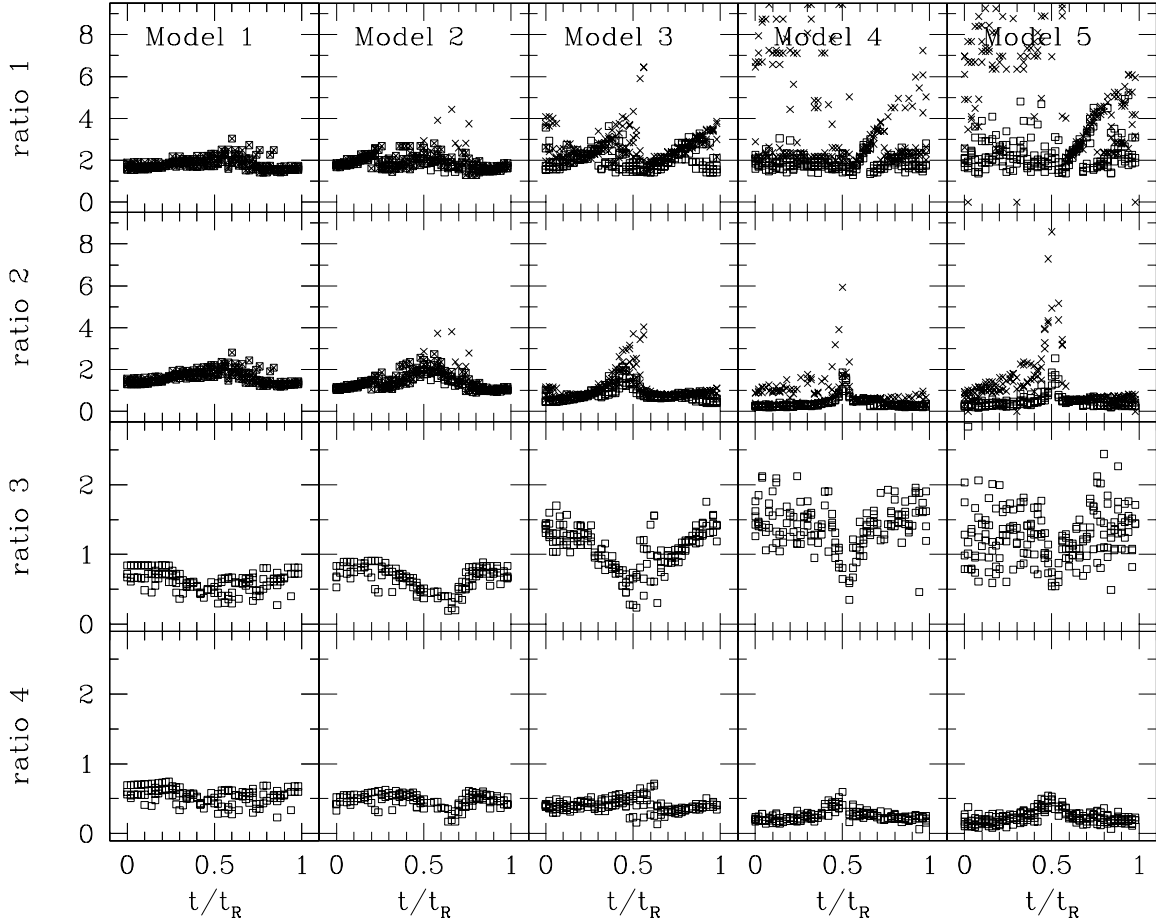


Fig. 15.— Ratio of  $r_{\text{break}}$  to  $r_{\text{tide,peri}}$  (“ratio 1”) and  $r_{\text{tide,inst}}$  (“ratio 2”) as a function of orbital phase (upper panels) for  $r_{\text{break}}$  defined using the limits  $\Delta\gamma_{\text{lim}} = 0.2$  (open symbols) and  $\Delta\gamma_{\text{lim}} = 1.0$  (crosses). Ratio of  $r_{\text{distort}}$  to  $r_{\text{tide,peri}}$  (“ratio 3”) and  $r_{\text{tide,inst}}$  (“ratio 4”) as a function of orbital phase (lower panels).

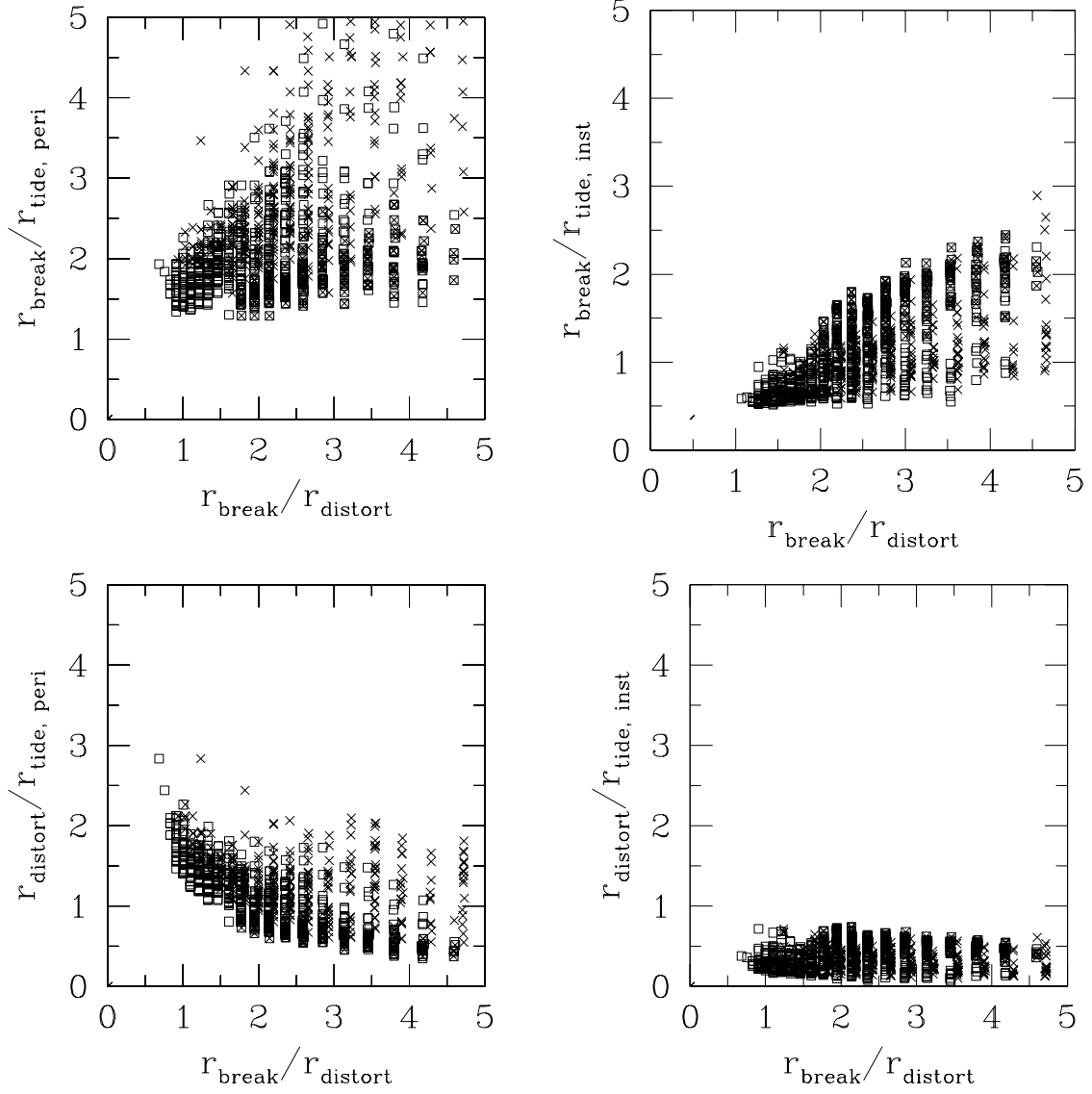


Fig. 16.— Ratio of  $r_{\text{break}}$  to  $r_{\text{tide,peri}}$  and  $r_{\text{tide,inst}}$  (upper panels) as a function of  $r_{\text{break}}/r_{\text{distort}}$  for  $r_{\text{break}}$  defined using the limits  $\Delta\gamma_{\text{lim}} = 0.2$  (open symbols) and  $\Delta\gamma_{\text{lim}} = 1.0$  (crosses). Ratio of  $r_{\text{distort}}$  to  $r_{\text{tide,peri}}$  and  $r_{\text{tide,inst}}$  as a function of  $r_{\text{break}}/r_{\text{distort}}$  (lower panels).



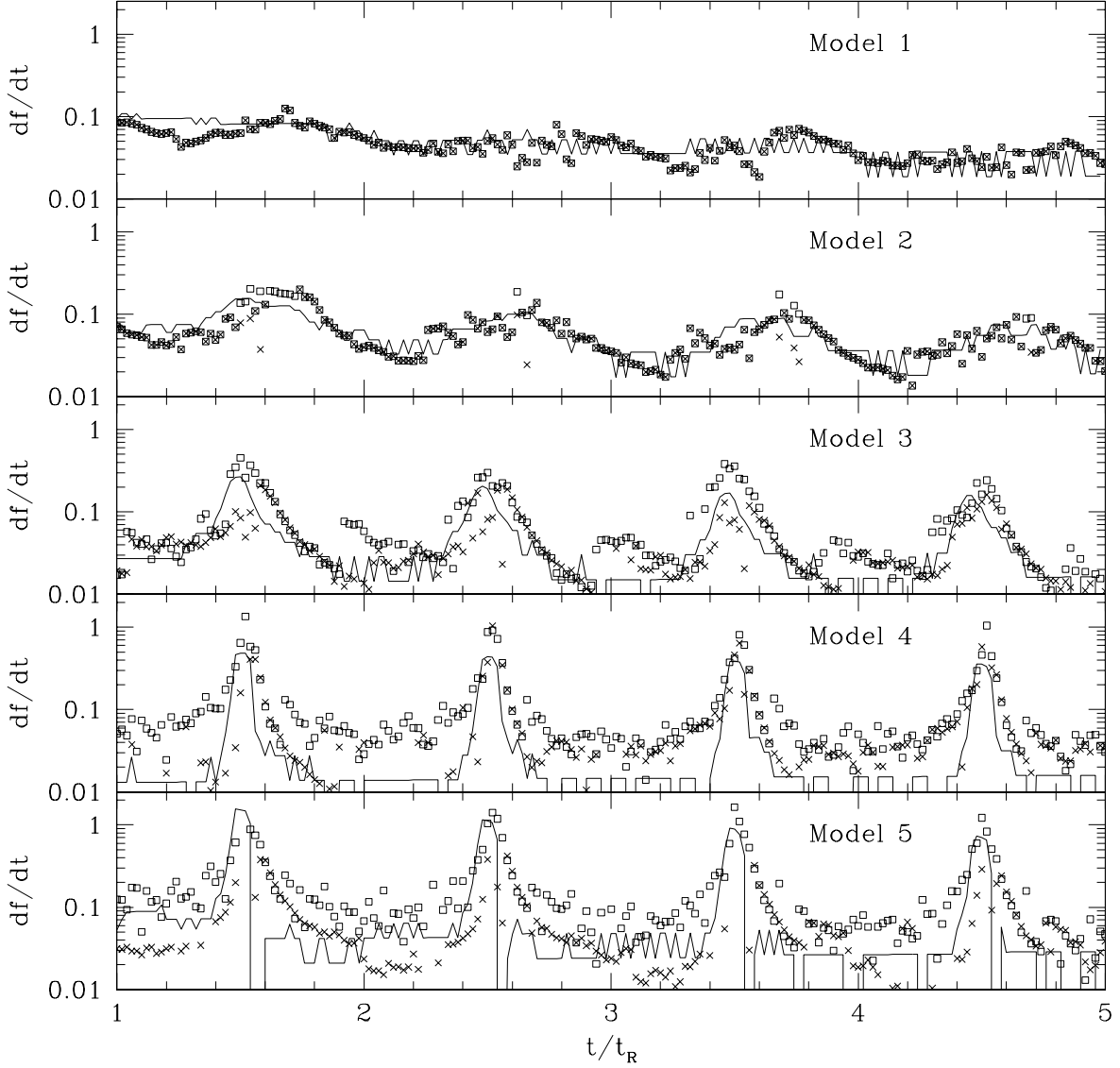


Fig. 17.— The solid lines represent the mass loss rate in the simulation and the boxes representing the mass loss rate estimated from equation (7) for  $r_{\text{break}}$  defined using the limits  $\Delta\gamma > 0.2$  (open symbols) and  $\Delta\gamma > 1.0$  (crosses).